

Volatile Organic Compound Detection Using Insect Odorant-Receptor Functionalised Field-Effect Transistors

by

Eddyn Oswald Perkins Treacher

A thesis submitted in fulfilment of the
requirements of the degree of
Doctor of Philosophy in Physics
School of Physical and Chemical Sciences
Te Herenga Waka - Victoria University of Wellington

Nov 2023



Table of contents

Acknowledgements	1
1. Fabrication of Carbon Nanotube Network and Graphene Field-Effect Transistors and Characterisation Methods	3
1.1. Introduction	3
1.2. Photolithography for Carbon Nanotube and Graphene Field-Effect Transistors	3
1.2.1. AZ® 1518 photoresist	5
1.2.2. AZ® nLOF 2020 photoresist	6
1.2.3. SU8-2150 photoresist	6
1.3. Fabrication of Carbon Nanotube and Graphene Field-Effect Transistors	7
1.3.1. General Remarks	7
1.3.2. Alignment Markers	10
1.3.3. Deposition of Carbon Nanotubes	10
1.3.4. Channel Etching	13
1.3.5. Source and Drain Electrodes	13
1.3.6. Encapsulation	16
1.4. Characterisation via Atomic Force Microscopy	20
1.5. Characterisation via Fluorescence Microscopy	21
1.6. Characterisation via Raman Spectroscopy	21
1.7. Electrical Characterisation	21
1.7.1. Sensing Measurements	24
1.8. Summary	25
2. Characteristics of Pristine Carbon Nanotube & Graphene Field Effect Transistors	27
2.1. Introduction	27
2.2. Carbon Nanotube Network Morphology and Composition	28
2.2.1. Atomic Force Microscopy	28
2.2.2. Raman Spectroscopy	34
2.3. Electrical Characteristics of Pristine Devices	36
2.3.1. Carbon Nanotube Network Devices	36
2.3.2. Graphene Devices	41
2.4. Real-Time Salt Concentration Sensing with Phosphate Buffered Saline	44
2.4.1. Control Series and Baseline Drift	44
2.4.2. Sensing Series	47

Table of contents

2.5. Conclusion	52
Appendices	55
A. Python Code for Data Analysis	55
A.1. Code Repository	55
A.2. Atomic Force Microscope Histogram Analysis	55
A.3. Raman Spectroscopy Analysis	55
A.4. Field-Effect Transistor Analysis	55

Acknowledgements

69450

Rifat, Alex - vapour sensor
Erica Cassie - FET sensing setup
Rob Keyzers and Jennie Ramirez-Garcia - NMR spectra
Patricia Hunt - Computational chemistry

1. Fabrication of Carbon Nanotube Network and Graphene Field-Effect Transistors and Characterisation Methods

1.1. Introduction

This chapter discusses the fabrication processes for both the carbon nanotube network and graphene field-effect transistors (FETs). Experimental optimisation of the transducer element is critical for biosensor work, and large numbers of transducers were required for testing various biosensor functionalisation processes. Therefore, these processes were developed to rapidly fabricate devices with reproducible device characteristics appropriate for biosensing work. Also outlined in this chapter are the characterisation techniques taken to test the quality and reproducibility of these fabrication processes.

The nitrogen ($\geq 99.99\%$) and oxygen (99.7%) used in fabrication work was supplied by BOC Limited New Zealand. All acetone and isopropanol used for wafer/device processing had a minimum 99.9% purity (HPLC grade). Deionised (DI) water was taken from a Synergy® UV Water Purification System. The DI water had a measured conductivity of $(1.4 \pm 0.1) \mu\text{S cm}^{-1}$, compared to tap water with a measured conductivity of $(7.8 \pm 0.2) \mu\text{S cm}^{-1}$.

1.2. Photolithography for Carbon Nanotube and Graphene Field-Effect Transistors

This section details some of the standard photolithography procedures used in the quarter wafer processing detailed in Section 1.3. Photoresists, also referred to here as “resists”, are UV light-sensitive polymeric resins used for photolithography. Both positive and negative photoresists were used in various fabrication processes. Positive resists are made soluble in alkalines by UV light exposure, meaning exposed areas are removed in the development process. Conversely, negative resists are cross-linked by exposure and a post-exposure bake step. The unexposed areas of the negative resist are then

1. Fabrication of Carbon Nanotube Network and Graphene Field-Effect Transistors and Characterisation

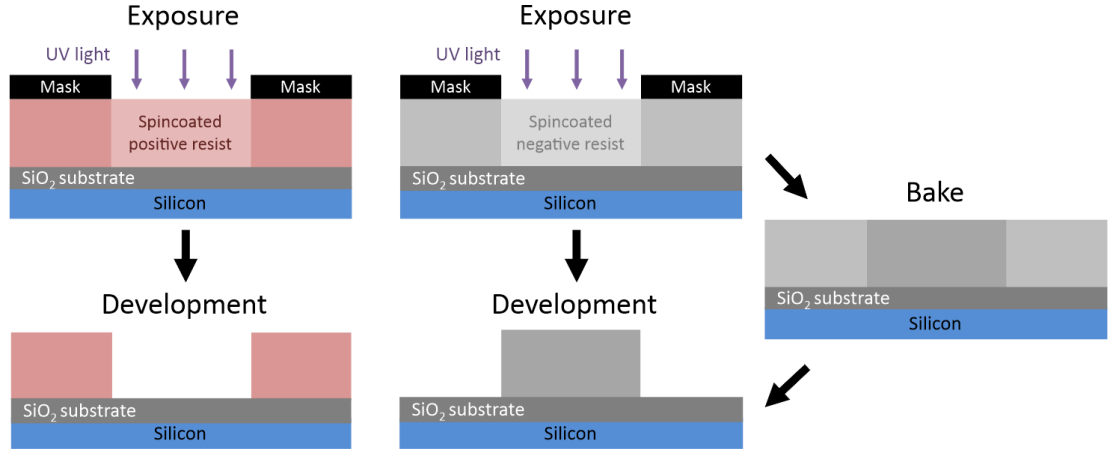


Figure 1.1.: A side-view comparison of generic photolithography processes for positive and negative resists in the ideal case. Photolithography with a positive resist requires a single softbake step before exposure, while for negative resists a second baking step is required after exposure (Thicknesses shown not to scale).

removed in the development process [1]. Figure 1.1 gives a visual representation of these differences.

The specific photoresist selected for photolithography depends on the specific use case. The types used in this thesis are positive and negative AZ® photoresists (AZ® 1518, Microchemicals GmbH; AZ® nLOF 2020, Microchemicals GmbH) and SU-8 (SU8-2150, Kayaku Advanced Materials, formerly Microchem). The AZ® resists used here have a minimum film thickness of $1.5 \mu\text{m}$ [1], while the SU8-2150 has a minimum film thickness of $0.5 \mu\text{m}$ [2]. Positive resists which have not been thermally crosslinked will soften at higher temperatures ($\gtrsim 100^\circ\text{C}$ for AZ® 1518), leading to a rounded profile. This is not the case for negative resists, which are more thermally stable [1]. Each resist therefore has a different cross-section profile, as shown in Figure 1.2.

If metal deposition is performed on a positive resist, some metal can collect on the outwardly-sloped sidewalls of the resist (see Figure 1.2) which forms significant spikes on the edges of the deposited metal upon lift-off. On the other hand, metal cannot collect on top of the inwardly-sloped negative profile sidewalls, which avoids the formation of large edge spikes. Therefore, the negative resist profile is more suited to metal or metal oxide deposition and lift-off processes, though the process is more sensitive to human error due to requiring more processing steps than positive resist [1]. Finally, when it is suitably processed SU-8 is considered to be more stable and biocompatible than other photoresists [3]. It is especially biocompatible when chemically modified via processes such as isopropanol sonication and O₂ plasma treatment [4].

All photolithographic exposure was performed using a Karl Suss MJB3 Contact Aligner

1.2. Photolithography for Carbon Nanotube and Graphene Field-Effect Transistors



Figure 1.2.: The overcut profile of a positive resist pattern is shown in (a). The undercut profile in (b) is ideal for thin-film metal deposition and subsequent patterned removal, known as “lift-off”. Each profile has had the central region of the substrate exposed to UV light prior to development.

with a USHIO super-high pressure 350 W mercury lamp (USH-350DS, Japan). When performing photolithography, the intensity reading from the aligner was 20.8 – 24.2 mW/cm² (Note however that an external photometer reading at 400 nm found an intensity output of 17.2 mW/cm² when the aligner read 21.0 mW/cm²).

In general, photolithography procedures should be performed under yellow lighting, as light wavelengths from 320 – 450 nm can promote reactions in the photoresist used. Aging of photoresist over time can also significantly affect the photolithography process, and therefore all processes should be re-optimised regularly over time to give the desired result [1]. The range in processing times for some steps of the processes used here are largely due to the effects of aging on the photoresist.

The step-by-step processes for each resist are detailed in the subsequent sections.

1.2.1. AZ® 1518 photoresist

1. Spincoat at a final speed of 4000 rotations per minute (rpm) for 1 minute, with an initial acceleration of 500 rpm/s (notes: clean the substrate with acetone, isopropanol (IPA) and nitrogen before spincoating; use only the minimum amount of photoresist required to fully cover the wafer surface; avoid any gaps or bubbles in the photoresist).
2. Softbake 2 – 4 minutes at 95°C on the hotplate (2 min for individual devices, 4 min for a quarter wafer)
3. Mask expose for 10 – 12 s (note: clean mask with acetone/IPA and N₂ dry before use)
4. Develop with 3 parts AZ® 326 (2.38 % TMAH metal-ion free developer, Microchemicals GmbH) in 1 part deionised (DI) water for 30 – 45 s (note: rinse for 10 – 15 s in one development solution, then perform the rest of the development

1. Fabrication of Carbon Nanotube Network and Graphene Field-Effect Transistors and Characterisation

- in clean developer for a cleaner profile; lightly agitate the solution throughout the development process)
5. Rinse device for 30 s in DI water to remove excess developer, then dry under nitrogen

1.2.2. AZ® nLOF 2020 photoresist

1. Spincoat at final speed of 3000 rotations per minute (rpm) for 1 minute, with an initial acceleration of 500 rpm/s (notes: clean the substrate with acetone, isopropanol (IPA) and nitrogen before spincoating; avoid any gaps or bubbles in the photoresist)
2. Softbake for precisely 60 s at 110°C on the hotplate
3. Mask expose for 2.7 – 3 s (note: clean mask with acetone/IPA and N₂ dry before use)
4. Post-exposure bake for precisely 60 s at 110°C on the hotplate to cross-link exposed resist
5. Develop with 3 parts AZ® 326 in 1 part DI water for 60 – 70 s (note: rinse for 30 s in one development solution, then perform the rest of the development in clean developer for a cleaner profile; lightly agitate the solution throughout the development process)
6. Rinse device for 30 s in DI water to remove excess developer, then dry under nitrogen

1.2.3. SU8-2150 photoresist

1. SU-8 was diluted in cyclopentanone until viscosity was low enough to spincoat on substrate and then sonicated at 50°C for 3 – 4 hours (Note: The dilution ratio used was ~1 part SU-8 to 5 parts cyclopentanone. However, the age of the SU-8 may mean that significant evaporation had occurred prior to use, and the amount of SU-8 actually present is underrepresented by this ratio)
2. Spincoat first with a final speed of 500 rpm (acceleration 500 rpm/s) for 10 seconds, followed by spincoating at 4000 rpm (acceleration 7500 rpm/s) for 40 s.
3. Softbake for 10 minutes at 95°C on the hotplate
4. Mask expose for 6 – 8 s (note: clean mask with acetone/IPA and N₂ dry before use)
5. Post-exposure bake for 10 minutes at 95°C on the hotplate to cross-link exposed resist

1.3. Fabrication of Carbon Nanotube and Graphene Field-Effect Transistors

6. Develop with SU-8 developer (Kayaku Advanced Materials, formerly Microchem) for 10 – 15 s, then clean in IPA for 30 s, repeat this step once then dry under nitrogen (note: lightly agitate the solution throughout the development process)

1.3. Fabrication of Carbon Nanotube and Graphene Field-Effect Transistors

1.3.1. General Remarks

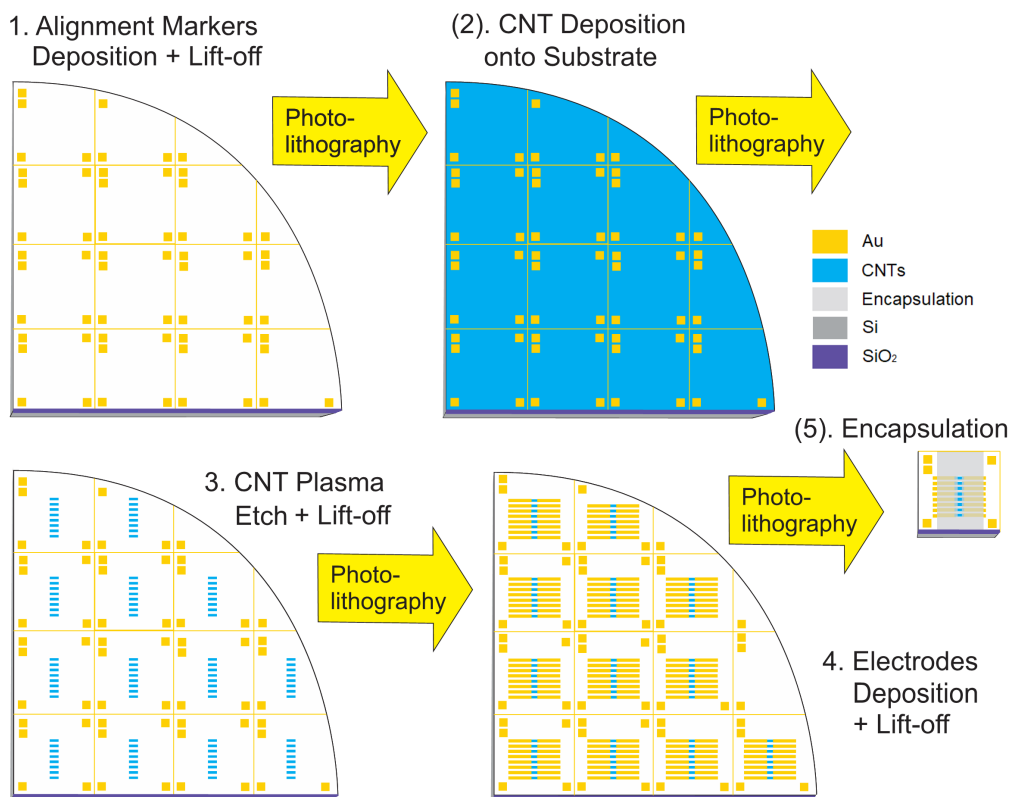


Figure 1.3.: The photolithographic processes used for fabrication of both carbon nanotube and graphene devices (graphene devices were fabricated individually for every step. Step #2 is passed over for graphene devices).

Photolithography was used to define eight channel regions on each device and subsequently to define metal contacts for each of these channels. A schematic demonstrating these photolithography processes on a quarter wafer is shown in Figure 1.3. Masks for photolithography were designed in-house using LayoutEditor CAD software and patterned externally with a UV laser writer.

1. Fabrication of Carbon Nanotube Network and Graphene Field-Effect Transistors and Characterisation

Thermal evaporation was used when depositing chromium (Cr-plated tungsten rods, Kurt J. Lesker) and gold (Au wire, 99.99%, Regal Castings Ltd.), while electron beam evaporation was used when depositing titanium (Ti pieces, 99.99%, Kurt J. Lesker) and metal oxides (*e.g.* Al₂O₃ pieces, 99.99%, Kurt J. Lesker). Metal and metal oxide deposition was performed using an Angstrom Engineering Nexdep 200 Vacuum Deposition System. Deposition thickness was monitored by a Inficon quartz piezoelectric sensor and controlled using an Inficon Deposition Controller. Electron beam power was provided by a Telemark TT-6 power supply. For metals, the chamber was initially evacuated to a pressure 5×10^{-6} mTorr, while for metal oxides the chamber was initially evacuated to a pressure of 1×10^{-5} mTorr. After evaporation, the chamber was cooled and vented with nitrogen.

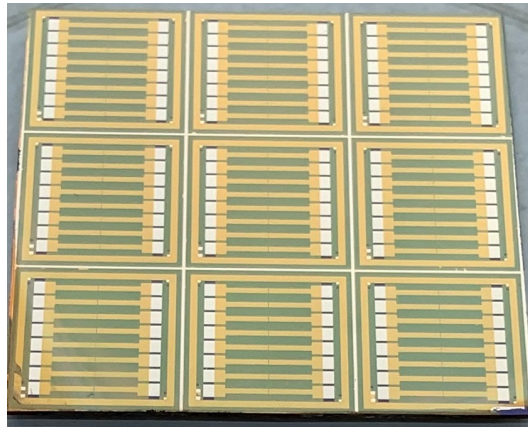
Carbon nanotube network field-effect transistors were fabricated using 4-inch *p*-type (B-doped) silicon wafers with either a 100 nm or 300 nm SiO₂ layer (WaferPro LLC) as the substrate. Devices intended for backgated measurements were fabricated with a 100 nm SiO₂ layer. Before photolithographic processing, the wafers were spin-coated with AZ® 1518 photoresist, placed photoresist-side down onto a cleanroom wipe, fixed in place using vacuum suction, then cleaved into quarters using a diamond-tipped scribe tool. For fabrication performed before June 2023, the protective photoresist layer was then removed by soaking the quarter-wafers in acetone for 15 minutes, then rinsed with isopropyl alcohol (IPA) and dried with N₂ gas. However, for complete removal of photoresist, we found it was necessary to flood expose the wafer with the Karl Suss Aligner for 1 min and then place it in AZ® 326 developer for 3 min, as discussed further in **?@sec-photoresist-contamination**.

Graphene field-effect transistors were fabricated using 300 nm SiO₂/p-type Si substrates covered with a monolayer of mechanically transferred CVD graphene (Advanced Chemical Supplier). This substrate was cleaved into equal-sized square chips before photolithography, with side length between 11.6 – 11.7 mm, subject to variability in wafer size. The same cleaving process outlined in Section 1.3.3 was used for cleaving the chips, but the photoresist was not rinsed off after cleaving. Devices were exposed to a brief burst of N₂ gas to remove any dust from the cleaving process from the surface of devices. When not being used in photolithography, graphene-based devices were stored in a vacuum desiccator to prevent the quality of the graphene deteriorating with exposure to air over time. The limited adhesion of graphene to the wafer meant that photolithographic processing had to be performed particularly carefully when fabricating graphene devices.

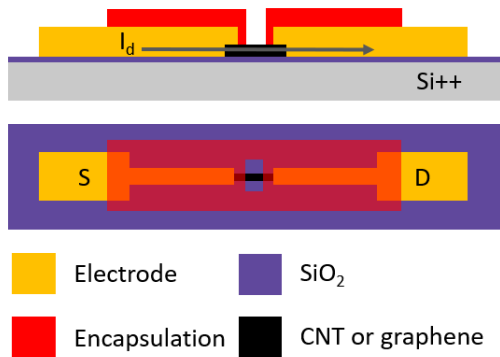
From Jul 2023 onwards, after each photolithography step using negative resist, quarter wafers/chips were placed in AZ® 326 or SU8 developer (depending on the type of resist) for 3 min to ensure complete removal of photoresist residue. For each step with positive resist, the same procedure was performed but with a flood exposure with UV light for 1 min before being placed in developer. The exception to this rule was for devices with an aluminium oxide layer present. Tetramethylammonium hydroxide (TMAH), the active ingredient of AZ® 326, etches through aluminium oxide and causes electrical shorts

1.3. Fabrication of Carbon Nanotube and Graphene Field-Effect Transistors

through the dielectric layer [5], [6]. A further discussion showing the results of this process is given in [?@sec-photoresist-contamination](#).



(a)



(b)

Figure 1.4.: A finished quarter-wafer with the unusable edges cleaved off is shown in (a). Note the double alignment markers feature in the bottom left corner of each device in (a), indicating channel 1 ‘CH1’. The component parts of the field-effect transistor are labelled on device cross-section and channel top view schematics in (b).

Figure 1.4a shows a completed quarter-wafer of carbon nanotube field-effect transistors, where partial (unusable) devices at the edges of the wafer have been cleaved off so that only a square of nine devices remains. An individual FET device after the completed fabrication process is shown in [?@fig-single-device-photo](#), and Figure 1.4b shows cross-section and top view schematics of the completed device with the component parts labelled.

1.3.2. Alignment Markers

Metal alignment markers were deposited in order to accurately align the device channels with device electrodes in subsequent photolithography steps. These alignment markers were asymmetric to indicate the orientation of the device for subsequent photolithography steps and electrical characterisation. In later discussion, channel 1 is defined as the channel placed closest to the large double square alignment marker feature. For carbon nanotube quarter wafers, alignment markers were deposited either directly before or after carbon nanotube deposition (see Section 1.3.3 for discussion). For graphene devices, alignment markers were deposited directly after cleaving using the protective photoresist layer spincoated prior to cleaving. AZ® 1518 was used for alignment marker photolithography.

For carbon nanotube devices made before Jun 2022, chromium was used as an adhesive layer for gold, while for all graphene devices and carbon nanotube devices made after Jun 2022, titanium was used as the adhesive layer. Metal layer thickness values quoted here are as stated on the Inficon controller. Without first corroborating these measurements with the Dektat profiler, these values should be treated as being strictly nominal. For chromium/gold depositions, 10 nm of chromium was deposited followed by a 100 nm Au layer. For titanium/gold depositions, a 10 – 20 nm of titanium was deposited followed by a 50 nm Au layer. Devices were then soaked in acetone for at least 2 hours for photoresist lift-off, washed in IPA and dried with nitrogen. The use of titanium gave rise to a cleaner lift-off and improved gold adhesion. Using a relatively thin gold layer (50 nm nominal instead of 100 nm) proved to still be clearly visible but to a cleaner lift-off. Profiler measurements of combined metal layer thicknesses after lift-off are described in Section 1.3.5.

1.3.3. Deposition of Carbon Nanotubes

Carbon nanotubes were deposited before the alignment markers photolithography step on all wafers fabricated between Aug 2021–Feb 2023, while devices fabricated before Aug 2021 and after Feb 2023 had the alignment markers photolithography step performed before the deposition of carbon nanotubes. The process order was first switched in Aug 2021 as this order led to faster processing times. However, the order was switched back in Feb 2023 to minimise the exposure of carbon nanotubes to photolithographic chemical processes.

Solvent-Based

The solvent-based deposition process for the carbon nanotube network in the second fabrication protocol is as follows. 10 mg of 2-mercaptopurine (99%, Sigma-Aldrich) was dissolved in 1 ml ethanol by sonication until clear. Quarter wafers were sonicated in acetone for 3 min, then exposed to O₂ plasma at 100 W for at least 2 min in a

1.3. Fabrication of Carbon Nanotube and Graphene Field-Effect Transistors

small plasma cleaner (Plasma Etch, Inc., PE-50 Compact Benchtop Plasma Cleaning System) or reactive ion etcher (Oxford Instruments, Plasmalab® 80 Plus) under 300 mTorr pressure. The cleaned SiO₂/Si surface was then coated with 2-mercaptopurine for 10 minutes, rinsed with ethanol to remove residual 2-mercaptopurine, and then nitrogen dried.

Meanwhile, 5 µg of 99% semiconducting carbon nanotube bucky paper (NanoIntegris, IsoNanotubes S-99) was dispersed in 10 mL of anhydrous 1,2-dichlorobenzene (DCB, Sigma Aldrich) by ultrasonication until no particles were visible to the naked eye. During this time, the ultrasonic bath temperature was kept between 20–30°C or the buckypaper would not disperse successfully. The substrates were then placed into a dish with CNT-DCB suspension and left covered for 1 hour, dipped into ethanol for 10 min to remove residual solvent and any unattached carbon nanotube bundles, and then dried with nitrogen. Devices fabricated using films deposited in this manner are sometimes referred to here as “solvent-deposited” networks.

Surfactant-Based

Two different approaches were used to attach the surfactant-dispersed carbon nanotubes (CNTs) to the substrate surface. The first approach was a simple drop-casting method, while the second was performed in the presence of steam ('steam-assisted'). In both approaches, the quarter wafers were first rinsed with ultrapure deionised water (DI water), acetone and IPA. Next, they were placed into a small plasma cleaner (Plasma Etch, Inc, PE-50 Compact Benchtop Plasma Cleaning System) or reactive ion etcher (Oxford Instruments, Plasmalab 80 Plus) and exposed to O₂ plasma at 100 W for at least 2 min under 300 mTorr pressure to make the surface hydrophilic. 1 mL of poly-L-lysine (PLL) was immediately deposited onto each quarter wafer and left for 5 minutes. The quarter wafers were then rinsed for 30 s with DI water and dried with N₂ gas. The presence of the PLL on the plasma cleaned surface strengthens the surface adhesion of semiconducting single carbon nanotubes after the surfactant dispersion has been dropcast onto the substrate.

For carbon nanotube network films deposited in surfactant without steam present, 2 mL of IsoNanotubes-S 90% or 99% dispersion (NanoIntegris) was decanted into a small bottle and sonicated for 5 s to break up bundles of CNTs. (Note: The composition of the surfactant used in the dispersion is proprietary to NanoIntegris.) An even spread of 400 µL carbon nanotube dispersion was placed in the centre of the PLL-functionalised quarter wafer, covered with a glass dish and left for 10 minutes. The dispersion was then rinsed off with DI water and IPA, and the quarter wafer was dried with N₂ gas. Next, the quarter wafer was annealed in a vacuum oven at 150° C for 1 hour to remove residual surfactant. This method would often lead to an inhomogeneous spread of CNTs across the quarter wafer surface, detailed further in section [?@sec-cnt-deposition-effects](#).

1. Fabrication of Carbon Nanotube Network and Graphene Field-Effect Transistors and Characterisation

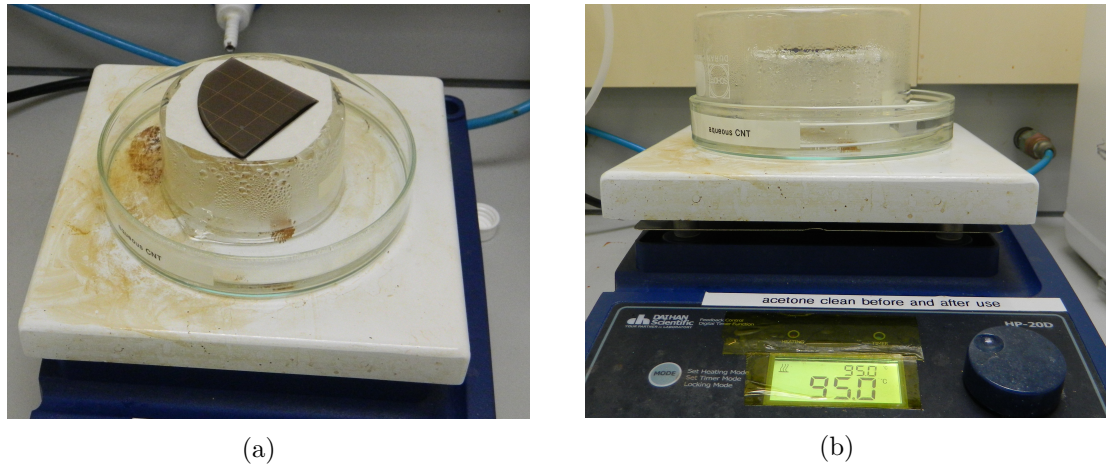


Figure 1.5.: Top view (a) and side view (b) of the steam-assisted method setup, with and without the glass steam cover above the quarter wafer.

For carbon nanotube network films deposited in surfactant in the presence of steam, 2 mL of IsoNanotubes-S 90% or 99% dispersion (NanoIntegris) was decanted into a small bottle and burst-sonicated once (on then off again) to break up bundles of carbon nanotubes. 75 mL of 95° C water was then placed into a glass dish on a hotplate held at 95° C. After this, the PLL-functionalised quarter wafer was placed in the centre of an insulating surface on the same hotplate. The carbon nanotube dispersion was carefully spread across the surface of the wafer without spilling any over the wafer edges. The wafer on the insulating surface and glass dish were then left under the same glass dish for 2 minutes to expose the wafer to steam from the glass dish. The use of an insulating surface meant that the wafer and dispersion were not heated from below while exposed to steam. The steam-assisted deposition setup is shown in Figure 1.5.

The carbon nanotube dispersion was then rinsed off the wafer with DI water, ethanol, acetone and IPA, and then the quarter wafer was dried with N₂ gas. As in the original method, the quarter wafer was then annealed in a vacuum oven at 150° C for 1 hour to remove residual surfactant. This method gave an even spread of CNTs across the quarter wafer surface, leading to a greater consistency in performance between devices. Further details can be found in [?@sec-cnt-deposition-effects](#). Devices fabricated using films deposited in this manner are sometimes referred to here as “steam-deposited” or “steam-assisted surfactant-deposited” networks (rather than simply “surfactant-deposited”, to avoid confusion with the steam-free method).

1.3.4. Channel Etching

Eight channel features, each 1000 μm in length and 100 μm in width with a pitch of 1200 μm, were patterned using AZ® 1518 photolithography on each carbon nanotube or

1.3. Fabrication of Carbon Nanotube and Graphene Field-Effect Transistors

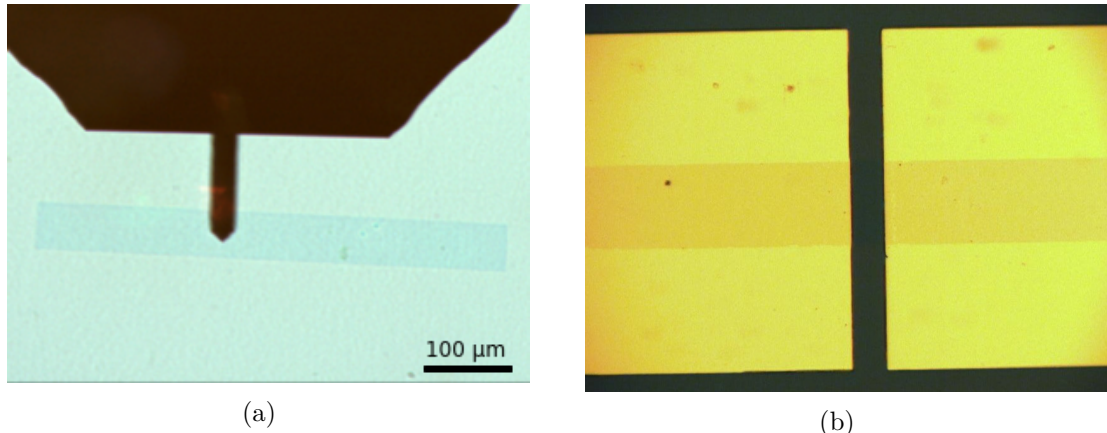


Figure 1.6.: A graphene channel after the plasma etch step is shown in (a), and (b) shows another graphene channel after the metal electrode deposition and liftoff step.

graphene-covered substrate. Unwanted nanomaterial not covered with photoresist was then etched away with 200 W oxygen plasma at 600 mTorr using a reactive ion etcher or RIE (Plasmalab® 80 Plus, Oxford Instruments). The etch time was 3 minutes for carbon nanotube quarter wafers, and 1 minute for graphene chips. The protective photoresist was then removed by soaking in acetone for at least 5 minutes.

1.3.5. Source and Drain Electrodes

The source and drain electrodes for each channel were patterned using photolithography with either AZ® 1518 photoresist (pre-Mar 2023) or AZ® nLOF 2020 photoresist (post-Mar 2023). Before metal deposition, the developed photoresist pattern was exposed to O₂ plasma at 50 W for up to 5 s or at 20 W for 20 – 25 s in a PE-50 plasma cleaner (Plasma Etch, Inc.) to remove residual photoresist on the developed regions and ensure a clean lift-off. After metal, wafers/devices were soaked in acetone for at least 2 hours for photoresist lift-off, washed in IPA and dried with nitrogen.

As with the alignment markers deposition (see Section 1.3.2), before Jun 2022 chromium was used for the gold adhesion layer, and after Jun 2022 titanium was used. Adhesion layers are required to stick metals such as gold and platinum to silicon dioxide [7]. A 20 nm nominal titanium layer instead of 10 nm nominal was found to give better electrode adhesion, and devices after Feb 2023 were made using this thicker adhesion layer. Good electronic contact could be made with electrodes with a nominal gold layer thickness of 60 – 100 nm, and a Au layer nominally 100 nm thick was most commonly used.

Dimethyl sulfoxide (DMSO) was sometimes used in electrodes lift-off instead of acetone between Jul 2021 and Feb 2023 because of its effectiveness as a photoresist stripping agent. However, it was abandoned due to some indications it was unsuitable for the

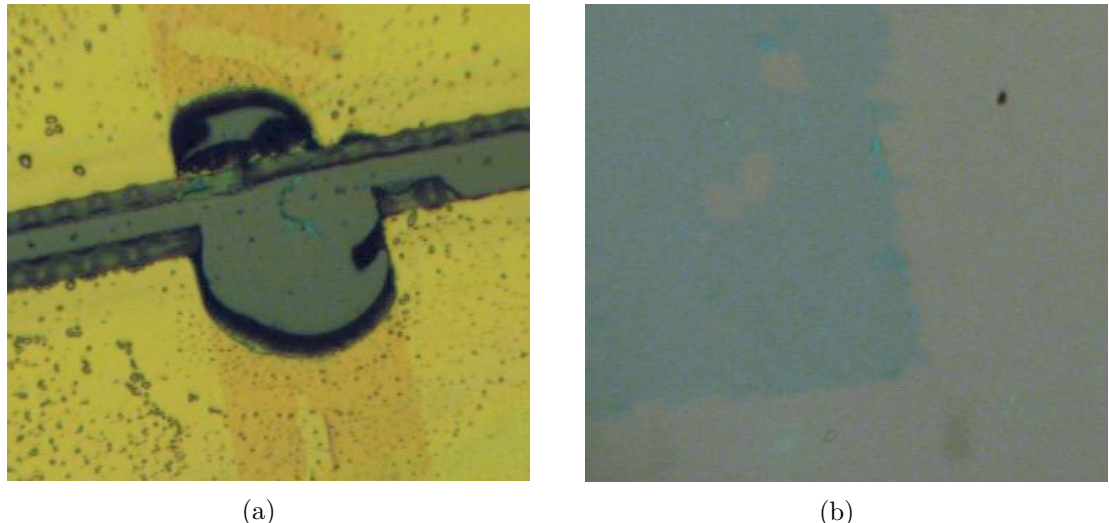


Figure 1.7.: Damage to the gold electrode in the graphene channel region after dimethyl sulfoxide lift-off is shown in (a), while (b) shows damage to a graphene film (blue-green region) after dimethyl sulfoxide lift-off.

devices being fabricated, as shown in Figure 1.7 and also as detailed in ?@sec-cnt-deposition-effects. It is possible that heat from the electrodes deposition sometimes crosslinked residual photoresist on the nanomaterial, and then during lift-off was removed together with any attached nanomaterial by the DMSO. However, it is also possible that prolonged exposure to DMSO alone was sufficient to detach nanomaterial from the substrate. Therefore, acetone was the preferred agent for lift-off despite being a less efficient stripping agent than DMSO.

Example height profiles of quarter wafer channels taken using a Veeco Dektat 150 profiler are shown in Figure 1.8. AZ® 1518 photoresist was used in Figure 1.8a and Figure 1.8b for photolithographic patterning. A 10 nm adhesion layer and 100 nm Au layer were used for each quarter wafers to ensure a consistent comparison. From these figures, we find an measured Cr/Au electrode height of 42 ± 1 nm and an measured Ti/Au electrode height of 48 ± 2 nm, slightly less than half the respective heights stated on the Inficon Deposition Controller.

Although using AZ® nLOF 2020 photolithography involves more processing steps, it gave rise to more cleanly-defined electrodes with a more consistent height profile. Often electrode deposition using AZ® 1518 photoresist would lead to sharp vertical spikes along the edge of the electrode, as seen in Figure 1.8c. These edge spikes or “cat ears” can partially or fully protrude through thin encapsulation materials such as SU8 and Al₂O₃, leading to significant leakage currents from the electrodes into the FET top gate. This effect is due to the profile of positive resists being suboptimal for lift-off processes, as discussed in Section 1.2.

1.3. Fabrication of Carbon Nanotube and Graphene Field-Effect Transistors

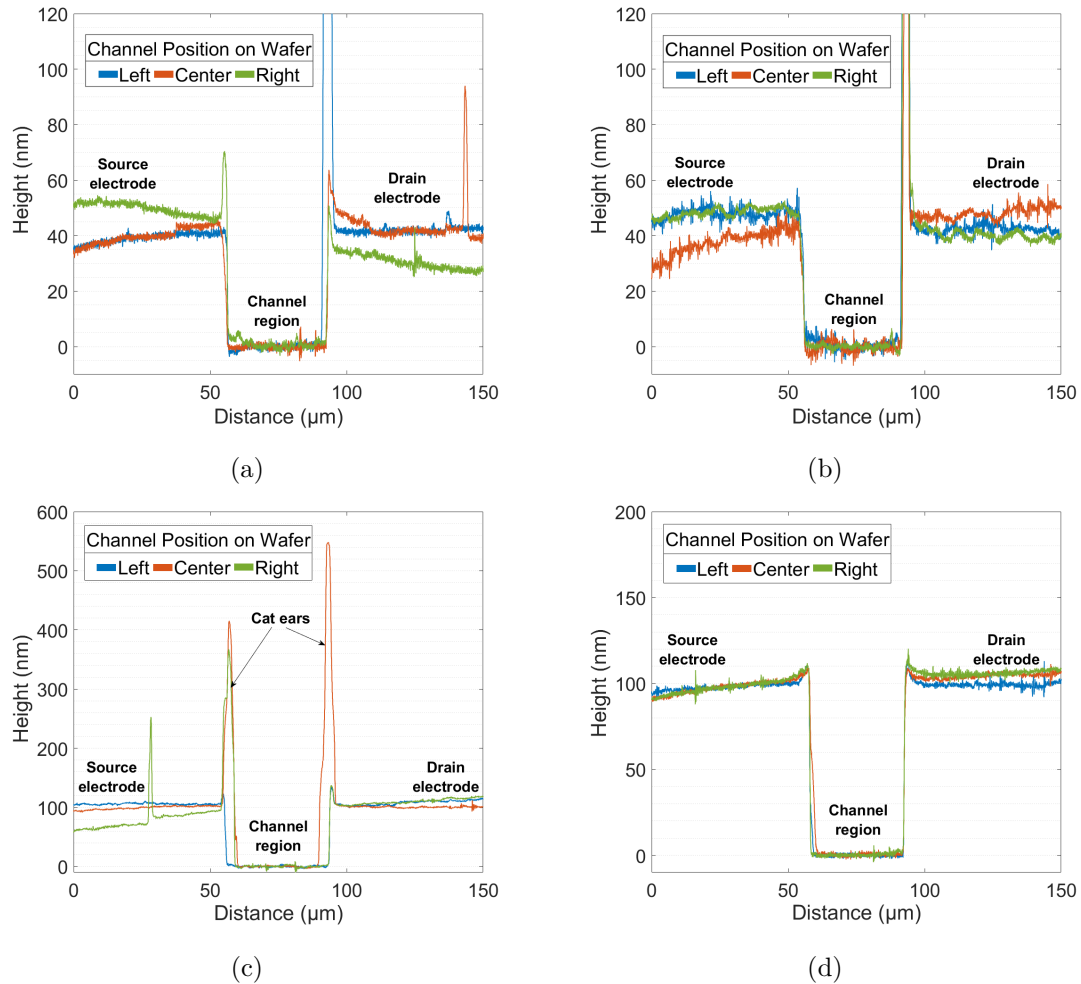


Figure 1.8.: The Dektat height profile measurements for source and drain electrodes taken at different locations on four different quarter wafers are shown here. A 10 nm adhesion layer and 100 nm Au layer were used for the wafers in (a) and (b), with chromium as the adhesion layer for (a) and titanium for (b). A 20 nm titanium adhesion layer and 100 nm Au layer were used for both (c) and (d). AZ® 1518 photolithography was used for patterning before metal deposition in (a)-(c), which led to the formation of edge features or “cat ears”, with (c) illustrating the full height of these features. In comparison, (d) shows the profile of electrodes from a quarter wafer patterned with AZ® nLOF2020, where edge features are greatly reduced.

1. Fabrication of Carbon Nanotube Network and Graphene Field-Effect Transistors and Characterisation

The height profile corresponding to a wafer with electrodes fabricated using AZ® nLOF 2020 is shown in Figure 1.8d. A 20 nm titanium adhesion layer and 100 nm Au layer were used for both Figure 1.8c and Figure 1.8d to ensure a consistent comparison, resulting in a measured electrode height of 103 ± 2 nm for both wafers. By comparing these figures, we see AZ® nLOF 2020 photoresist has a more consistent electrode height profile across the wafer surface than the wafer which used AZ® 1518 resist. The measured edge features for the AZ® 1518 resist electrodes vary in size from 20 nm to 450 nm above the bulk electrode surface, whereas the edge features for the AZ® nLOF 2020 resist do not exceed 14 nm in height.

1.3.6. Encapsulation

Several different approaches were used for the encapsulation, or contact protection, of devices. The encapsulation of graphene and carbon-nanotube transistors for biosensing is essential to improve transistor characteristics, passivate the electrodes and ensure only the nanomaterial region is active during biosensing, as discussed in [?@sec-biosensor-methods](#).

Before encapsulation photolithography the carbon-nanotube network quarter wafers were cleaved into individual 11 mm \times 11 mm chips, using the cleaving process outlined in Section 1.3.3. Cleaving the devices at this step simplified mask alignment and ensured consistent thickness across photoresist encapsulated devices.

Two different photolithography masks were used for encapsulation photolithography in this work, with different exposed areas of active nanomaterial. The first mask was used for devices made before Jan 2023, and was designed to leave a region of 500 $\mu\text{m} \times 10 \mu\text{m}$ unencapsulated for each channel. The second mask was used exclusively after Jan 2023, and was designed to leave a region of 200 $\mu\text{m} \times 20 \mu\text{m}$ unencapsulated for each channel. This change was made to double the area of carbon nanotubes exposed to electrolyte while halving the area of SiO₂ dielectric exposed to electrolyte during aqueous sensing.

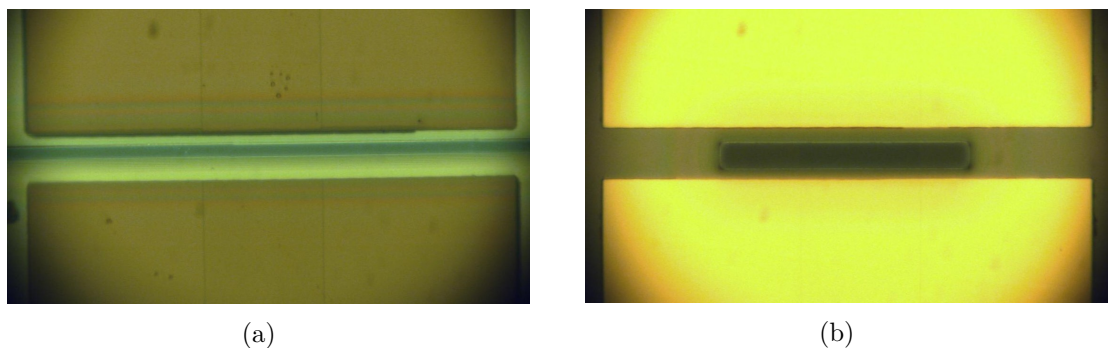


Figure 1.9.: Figures showing encapsulation with hardbaked AZ® 1518 using the pre-2023 mask in (a), and the 2023 mask in (b).

1.3. Fabrication of Carbon Nanotube and Graphene Field-Effect Transistors

A side-by-side microscope comparison of hardbaked AZ® 1518 processed with each mask is given in Figure 1.9, while a Dektat profile comparison corresponding to Figure 1.9 is shown in `?@fig-old-new-mask`. The profiles corresponding to the mask used after Jan 2023 clearly exhibit greater device-to-device consistency, partly due to the mask requiring a greater level of accuracy when aligning the encapsulation pattern with the electrode channel. The larger feature size also means development time has less of an impact on the quality of the encapsulation opening.

Photoresist encapsulation

Two types of photoresist were initially trialled for encapsulation of carbon nanotube network devices, AZ® 1518 and SU8-2150. Both AZ® 1518 [8]–[10] and SU-8 have been previously used for device encapsulation, with SU-8 noted for being particularly stable and biocompatible [3], [4], [11].

Once developed, the photoresist pattern was exposed to O₂ plasma at 50 W for up to 5 s or at 20 W for 20 – 25 s to remove excess photoresist from the encapsulation opening. Devices were then hardbaked at 200°C for 1 hour to fully crosslink the encapsulation layer. This crosslinking ensured subsequent device exposure to solvent did not remove the photoresist encapsulation.

The exposed region clear of AZ® 1518 resist was $6.8 \pm 0.3 \mu\text{m}$ in width when using the old, pre-2023 mask, while the exposed region was $16.6 \pm 0.4 \mu\text{m}$ when using AZ® 1518 with the new mask from 2023, as seen in Figure 1.10a and Figure 1.10b. However, the exposed region was reduced for the SU-8 encapsulation relative to the AZ® 1518, with an width of only $3.6 \pm 0.5 \mu\text{m}$ for the pre-2023 mask, as seen in Figure 1.10d. Photoresist development using SU-8 was significantly more time-sensitive than for the AZ® 1518. This meant when the development time was increased to create a wider encapsulation opening, it was difficult to avoid removing large areas of photoresist across the entire surface of the encapsulation. This meant using the new mask from 2023 was especially important for maximising the exposed channel region of SU-8 devices. From Figure 1.10c, we see the new mask from 2023 with the SU-8 resist gave a significantly improved width of $13.8 \pm 1.0 \mu\text{m}$ for the exposed region.

A relatively thin SU-8 encapsulation layer could be deposited when compared to the AZ® 1518 encapsulation profile. From Figure 1.10, we see that the AZ® 1518 encapsulation layer had a average height of $1.7 \pm 0.2 \mu\text{m}$, while the SU-8 encapsulation layer had a average height of $680 \pm 20 \text{ nm}$. The SU-8 also had much less significant edge features than the AZ® 1518, regardless of the profiles of the source and drain electrodes.

As noted previously, for both resists the overall profile was more consistent for the new, 2023 mask from device to device than for the old pre-2023 mask.

AZ® 1518 encapsulation was used for all graphene devices fabricated.

1. Fabrication of Carbon Nanotube Network and Graphene Field-Effect Transistors and Characterisation

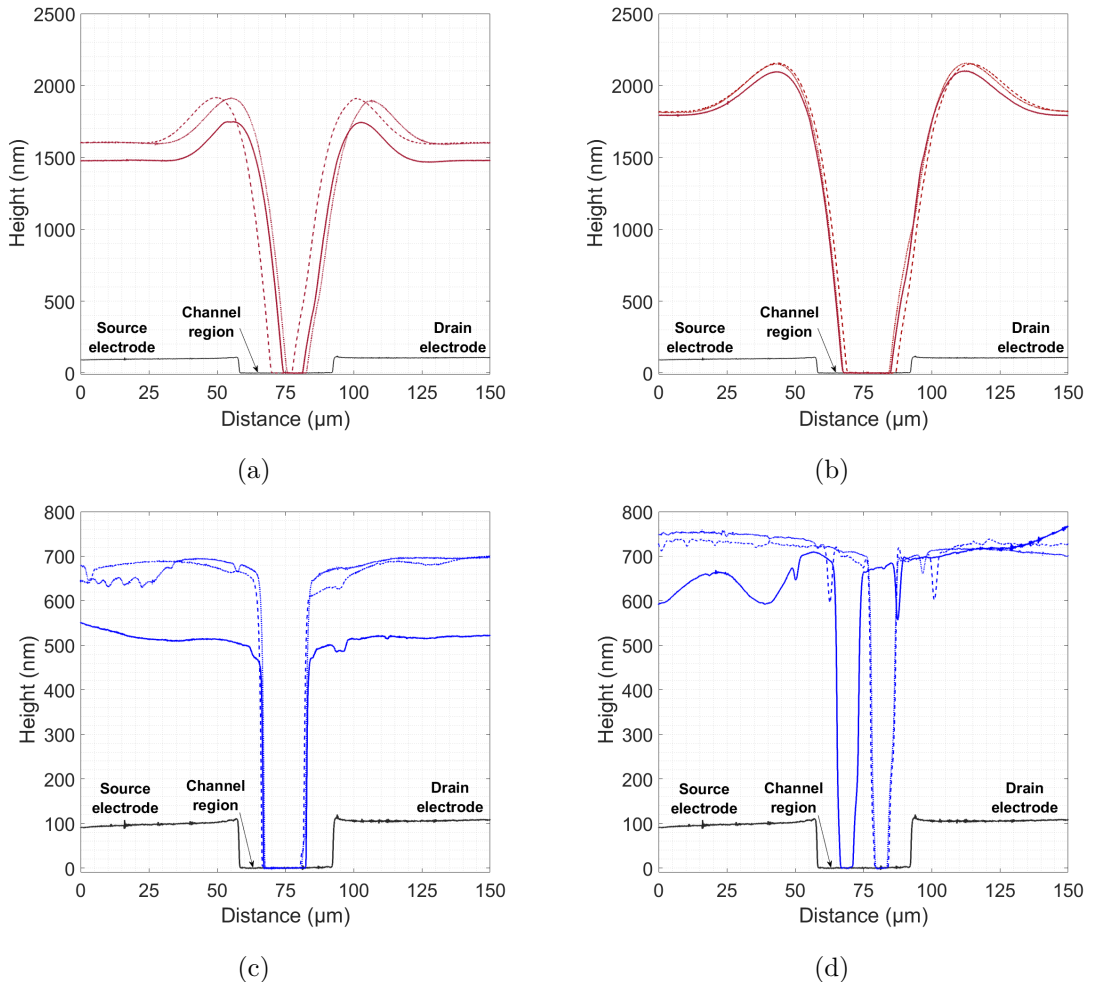


Figure 1.10.: Dektat of carbon nanotube devices after encapsulation photolithography using hardbaked AZ® 1518 and SU-8 2150, taken from various devices. (a) and (c) show photolithography performed with the old, pre-2023 mask, using AZ® 1518 and SU-8 2150 respectively. (b) and (d) show photolithography performed with the new mask from 2023 onwards, using AZ® 1518 and SU-8 2150 respectively.

1.3. Fabrication of Carbon Nanotube and Graphene Field-Effect Transistors

Dielectric encapsulation

Another approach taken was encapsulation of electrode channels with a dielectric metal oxide/ceramic layer. A electron beam deposition process was used to deposit a 100–150 nm nominal metal oxide layer on devices patterned with the 2023 mask using AZ® nLOF 2020 photoresist. As in Section 1.3.5, the developed photoresist pattern was exposed to O₂ plasma at 50 W for up to 5 s or at 20 W for 20 – 25 s in a PE-50 plasma cleaner (Plasma Etch, Inc.) before ceramic deposition. Before May 2023, devices were left in TechniStrip® MLO 07 (MicroChemicals) for 5 – 10 min for lift-off. However, due to concerns over the impact of the constituent chemical DMSO on the nanomaterial region (see Figure 1.7), the lift-off process was altered from May 2023 onwards. After May 2023, devices were soaked in acetone for at least 4 hours and sonicated in clean acetone for 30 – 60 s to lift-off the photoresist, then washed in IPA and dried with nitrogen.

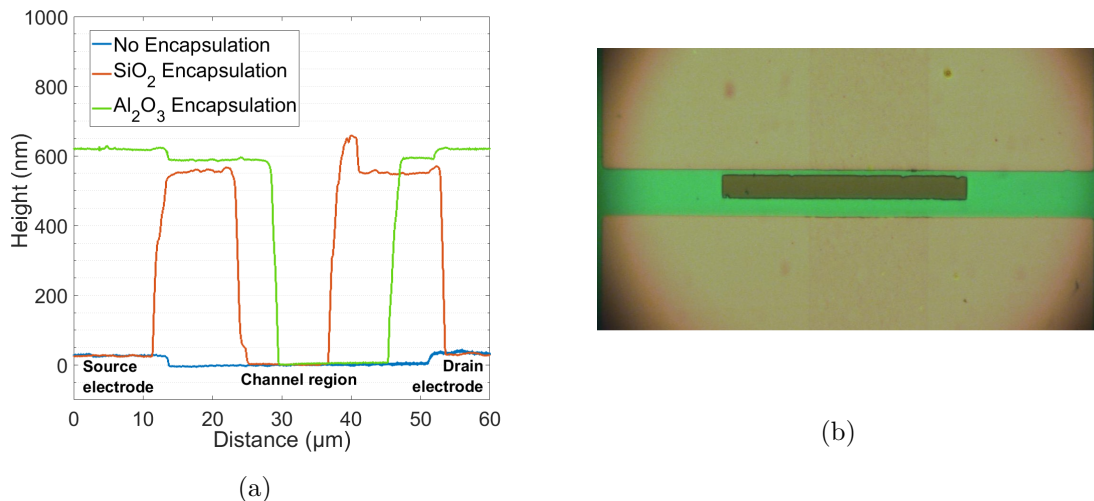


Figure 1.11.: A profile comparison of dielectric materials used for encapsulation is shown in (a), alongside a microscope image of a device encapsulated with aluminium oxide in (b). Note that the layer thicknesses in (a) were from initial tests of the process and are used for illustrative purposes.

The initial attempt at fabricating a dielectric encapsulation layer used silicon dioxide as the dielectric. However, silicon dioxide adheres poorly to gold without an metallic adhesive layer present, as shown in Figure 1.11a. Aluminium oxide was chosen as an alternative as it sticks well to bulk electrode materials, is heat and chemical resistant, has a relatively high dielectric constant and is bio-compatible [3], [7], [12]. Figure 1.11 shows the aluminium oxide successfully adhered to the electrodes and had a clean profile comparable to that of the SU-8 encapsulation layer after lift-off.

Unfortunately, when aluminium oxide layers which were thicker than ∼100 nm were deposited, there was found to be a significant drop in current relative to the unencapsulated

1. Fabrication of Carbon Nanotube Network and Graphene Field-Effect Transistors and Characterisation

device. This drop was significant enough to make devices unsuitable for sensing. Meanwhile, devices with encapsulation ~ 100 nm thick had significant gate current leakage through the encapsulation layer when liquid-gated. This leakage was present even when AZ® nLOF 2020 was used for electrode patterning to avoid edge spikes (as discussed in Section 1.3.5). Furthermore, aluminium oxide should not be subsequently exposed to its etchant TMAH, meaning it was difficult to completely remove residual photoresist from device channels after encapsulation. Possible future approaches to ceramic encapsulation are discussed in [?@sec-future-work](#).

1.4. Characterisation via Atomic Force Microscopy

Atomic force microscopy in this thesis was taken using a Nanosurf NaioAFM in dynamic force mode (also known as tapping mode, oscillating mode, acoustic AC mode or intermittent-contact mode). An ACLA probe (AppNano) was used with a tip diameter of 12 nm, height of 14 – 16 μm and a nominal cantilever spring constant of 58 N/m. All atomic force microscopy was performed with the Nanosurf NaioAFM on a stabilising table under a Faraday cage to minimise mechanical and electromagnetic interference. A 256×256 pixel resolution was typically used. Imaging was performed in air at room temperature.

Atomic force microscope (AFM) images could not be taken from the small exposed channel region on the encapsulated devices, so were instead taken on a representative carbon nanotube or graphene film sample fabricated on the same wafer as the device being tested. Moisture adversely affected the AFM imaging process. Therefore, films functionalised with biological materials were washed with DI water and gently dried with N_2 before atomic force microscope images were taken.

The open source data analysis software Gwyddion (version 2.59) was used to analyse AFM images. This included levelling the background with the polynomial background removal function, removing scarring and zeroing the z-scale.

1.5. Characterisation via Fluorescence Microscopy

Fluorescence microscopy was performed using an Olympus BX63 fluorescence microscope controlled using cellSens imaging software. Microscope objectives used were all Olympus UPLSAPO/UPlanSApo, apochromat objectives which compensate for spherical and chromatic aberrations. Objectives had infinite aperture and a field number of 26.5. Filter cubes used included the Olympus FITC filter (excitation wavelength range: 467 – 498 nm, emission wavelength range: 513 – 556 nm), Texas Red (excitation wavelength range: 542 – 582 nm, emission wavelength range: 604 – 644 nm) and GFP (excitation wavelength range: 604 – 644 nm, emission wavelength range: 502 – 538 nm). The ISO was kept at the lowest available setting, ISO200. All microscopy was performed

1.6. Characterisation via Raman Spectroscopy

in darkness with the screen turned away from the microscope. To ensure photobleaching did not adversely affect imaging, images were taken soon after initial exposure to fluorescence and taking repeated photos of the same region was avoided. Various useful and thorough introductions to fluorescence microscopy can be found online [13], [14].

1.6. Characterisation via Raman Spectroscopy

Raman spectroscopy was performed with a HORIBA Jobin Yvon LabRAM HR800 Raman spectrometer. The wavelength and power used for laser excitation of samples were 514 nm and 1 mW respectively. Spectra were taken with a 1800 line holographic grating with a hole size of 300 μm . A accumulation time of 20 seconds was used when taking spectra. Each spectrum was recorded twice at nine positions on device film, with a minimum distance of 10 μm between each position. Spectra were collected over two wavenumber ranges at each position, with the first range between 100 cm^{-1} and 650 cm^{-1} , and the second between 1300 cm^{-1} and 1650 cm^{-1} .

1.7. Electrical Characterisation

Both liquid-gated and back-gated measurements were taken of carbon nanotube and graphene devices. Liquid-gated measurements were taken using the configuration shown in Figure 1.12. Back-gated measurements were taken with a copper plane placed underneath the Si/SiO₂ wafer and connected to SMU 3 instead of the reference electrode.

All measurement setups used had the same basic configuration, with two source measure units (SMUs) attached to the source and gate. Voltage from the source and gate SMUs was either kept constant or varied, with only one SMU varied at a time. Three different measurement setups were used for taking these measurements, the Agilent (Keysight/HP) 4156C Semiconductor Parameter Analyser, the Keysight B1500A Semiconductor Device Analyser, and a National Instruments NI-PXIe modular measurement system with a 8 GB PXIe-8821 controller and two NI-4138 source measure units. For measurements with the Keysight instruments, a third, drain SMU was attached and kept at a constant 0 V (as shown in Figure 1.12).

When using the Agilent 4156C Semiconductor Parameter Analyser or Keysight B1500A Semiconductor Device Analyser for liquid-gated measurements, a Rucker and Kolls with micromanipulators was used to contact the devices; when using the National Instruments NI-PXIe for liquid-gated measurements, a custom-made chip carrier with spring-loaded, pointed-tip, gold-coated pogo pins was used. Ag/AgCl standard electrodes were used as the liquid-gate electrode. The electrode was submerged in 80 μL of PBS buffer in a polydimethylsiloxane (PDMS) ‘well’ – a flexible structure used to contain the electrolyte solution – with outer dimensions of 12 mm \times 6 mm \times 6 mm. This PDMS well was sonicated in isopropanol for 10 min and thoroughly N₂ dried before use. The microscope

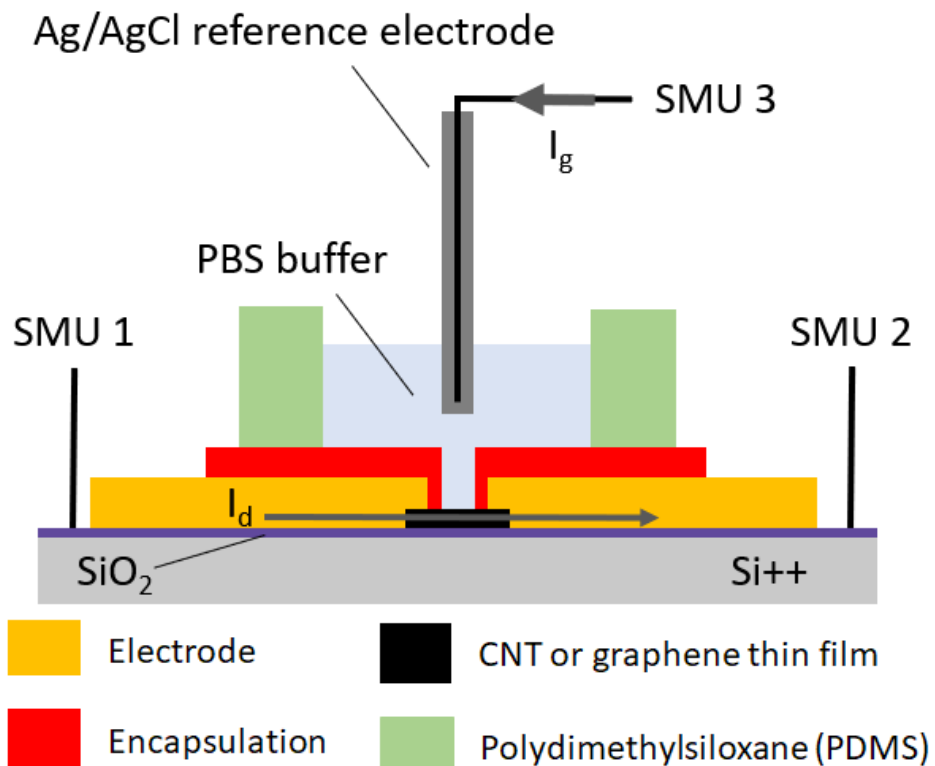
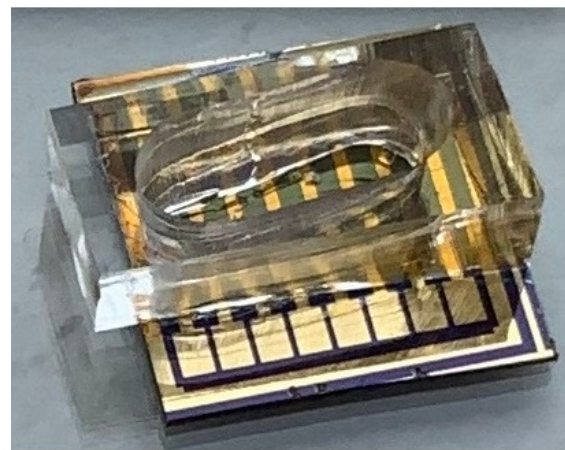
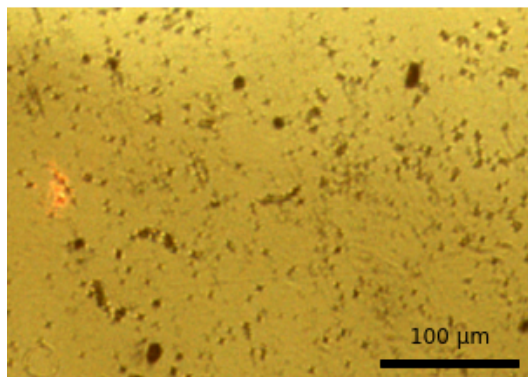


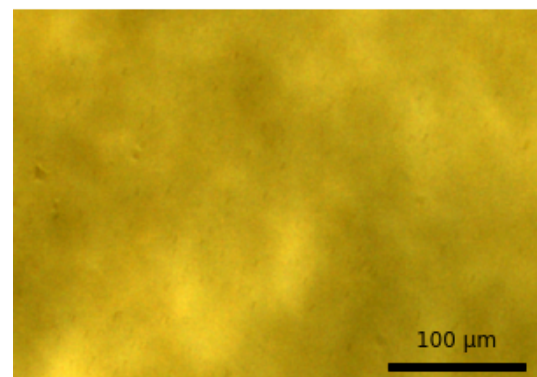
Figure 1.12.: Liquid-gated device schematic showing electrical connections to the three source measure units. V_{ds} is applied between the source SMU (SMU 1) and the drain SMU (SMU 2), while V_{lg} is applied between the gate SMU (SMU 3) and the drain SMU. The drain SMU is held at 0 V or connected to a ground plane. Drain current I_d is measured at the drain SMU, and gate leakage current I_g is measured at the gate SMU.



(a)



(b)



(c)

Figure 1.13.: A carbon nanotube field-effect transistor device with a polydimethylsiloxane (PDMS) ‘well’ placed on the device surface is seen in (a), followed by microscope images of the surface of a well before (b) and after (c) isopropanol (IPA) sonication for 10 minutes.

1. Fabrication of Carbon Nanotube Network and Graphene Field-Effect Transistors and Characterisation

images seen in Figure 1.13 show the PDMS surface before and after this cleaning step. The end of Ag/AgCl standard electrode to be submerged should be rinsed in DI water and left to sit in DI water for 15 minutes before characterisation is performed.

The Agilent 4156C Semiconductor Parameter Analyser and Keysight B1500A Semiconductor Device Analyser were also used for back-gated measurements of devices within the vapour delivery system device chamber. When the lid of this chamber was tightly sealed, it acted a Faraday cage for another custom-made chip carrier with spring-loaded gold-coated pogo pins, able to contact four channel electrode pairs at once. The silicon back of the device was pressed by the pins against a copper block, connected to the gate SMU.

Custom programs for National Instruments LabView 2017 were used for measurements from the Agilent 4156C Semiconductor Parameter Analyser and the National Instruments NI-PXIe. Keysight EasyEXPERT software was used for characterisation with the Keysight B1500A Semiconductor Device Analyser.

Liquid-gated transfer characteristics of carbon nanotube FETs were measured at $V_{ds} = 100$ mV and liquid-gated transfer characteristics of graphene FETs were measured at $V_{ds} = 1$ V, where V_{lg} was swept between -0.5 V and 1 V in both the forward and reverse direction with a step size of either 10 or 20 mV. Backgated transfer characteristics of carbon nanotube FETs were either measured at $V_{ds} = 100$ mV or $V_{ds} = 1$ V, where V_{bg} was swept between -5 V and 5 V or -10 V and 10 V in the forward and reverse directions with a step size of 50 mV or 100 mV.

1.7.1. Sensing Measurements

A liquid-gated setup was used for aqueous-phase sensing and a back-gated setup in the vapour delivery system was used for vapour-phase sensing, as described above.

Sensing measurements were performed with constant source-drain and gate voltages. The gate voltage used was chosen by locating the subthreshold region of the device transfer characteristics and choosing a voltage that fell within this region, usually $V_g = 0$ V.

Using the NI-PXIe with the PXIE-2737 module, eight-channel multiplexed current measurements could be taken in rapid succession. An integration time of 200 or 400 ms was used for sampling with each channel, with the actual sampling rate set by the NI-PXIe. In practice this meant a sampling rate of 1.81 s (for 200 ms integration time) or 3.41 s (for 400 ms integration time) for any given channel. A 200 ms integration time meant the time between samples from successive channels varied between 220ms – 230 ms, while a 400 ms integration time meant the time between samples was consistently 426 ms. The Keysight equipment used a constant 1 s sampling interval.

Aqueous Sensing

Before the sensing process, 200 μL of PBS was added to the PDMS well and 100-120 μL of PBS was removed. This initial step was performed to wet the sides of the PDMS well, and check that the attachment of the PDMS well to the device would not unseal when larger volumes of PBS were added during sensing. Before any sensing measurement, a transfer characteristic curve was taken of the liquid-gated device. The initial amount of buffered electrolyte in the well was 100 μL , unless specified otherwise.

From February 2022 onwards, the standard sensing addition series used comprised of a ‘control series’ and an ‘analyte sensing series’. The control series was performed as part of each sensing experiment to test for unwanted responses to electrolyte and to allow baseline drift to settle. The total control series interval was 1800 s. Electrolyte additions of 20 μL were made at 100 s, 200 s and 300 s, while electrolyte subtractions of 20 μL were made at 400 s, 500 s and 600 s. Immediately after the control series, a sensing sequence was performed as part of the same continuous measurement set. An initial electrolyte addition was performed at 2100s, to confirm no changes occurred during the control series that would interfere with sensing. Unless specified otherwise, five analyte additions were then made with a time spacing of 300 s, at 2400 s, 2700 s, 3000 s, 3300 s and 3600 s. The experimental series was set to finish at 4000 s. The exact timings, analyte concentrations and gate voltage used in a given sensing sequence are discussed alongside the relevant experimental results.

Vapour Sensing

A variety of vapour sensing sequences were used in this work, which are discussed in [?@sec-vapour-sensing-biosensors](#) in detail.

1.8. Summary

A variety of approaches were trialled when depositing a carbon nanotube network for the fabrication of transistor devices, and the resulting morphologies of these networks are discussed in the next chapter. Standard photolithographic methods were used to successfully fabricate carbon nanotube and graphene field effect transistor devices. A range of photolithography types and electrode/encapsulation materials were trialled to find the optimal device composition for sensing, also discussed in the next chapter. Atomic force microscopy, fluorescence microscopy and a variety of electrical measurement setups were used to characterise the devices.

2. Characteristics of Pristine Carbon Nanotube & Graphene Field Effect Transistors

2.1. Introduction

A range of methods were followed to fabricate carbon nanotube network and graphene field-effect transistors for biosensor use. This chapter therefore looks to use the characterisation techniques outlined in the previous chapter to compare and contrast the device channel morphologies and electrical characteristics resulting from various methods.

The three carbon nanotube film types used for devices were the solvent-deposited, surfactant-deposited and steam-assisted surfactant-deposited (steam-deposited) films discussed in the previous chapter. As minor changes were made to fabrication processes throughout the thesis, the fabrication dates of devices used are stated, which can be cross-referenced with Chapter 1 to identify the specific process used. Atomic force microscopy and Raman spectroscopy was performed on the carbon nanotube networks to identify the distribution of carbon nanotube diameters and the defects present on the carbon nanotube networks. Electrical characterisation was then used to see how the morphology of each film type affects the performance of the completed devices. Both back-gated and liquid-gated transfer characteristics were compared, as well as key parameters taken from the liquid-gated characteristics. The electrical behaviour of liquid-gated graphene devices was also examined, as well as the impact of water on the performance of back-gated devices for vapour sensing use.

Finally, as a control measurement for liquid-gated sensing and to verify the behaviour of the pristine device as a sensor, a salt concentration sensing series was performed with a steam-deposited carbon nanotube network device. The device characteristics were taken and device drift was examined and modelled. The sensing series was performed by successively diluting 1XPBS electrolyte in the polydimethylsiloxane ‘well’ (electrolyte container) while passing a current through the device, and measuring the current response to dilutions. Various filters were applied to the collected data to better understand the signal change.

2.2. Carbon Nanotube Network Morphology and Composition

2.2.1. Atomic Force Microscopy

Figure 2.1 shows a side-by-side comparison of the surface morphology of carbon nanotube films fabricated using the methods described in Section 1.3.3. These images were collected using an atomic force microscope and processed in the manner described in Section 1.4. Figure 2.1a shows a film of carbon nanotubes deposited in solvent, Figure 2.1c shows a film of carbon nanotubes dropcast in surfactant, and Figure 2.1e shows carbon nanotubes dropcast in surfactant in the presence of steam. As discussed in previous works using solvent-based deposition techniques for depositing carbon nanotubes, in each network multi-tube bundles form due to strong mutual attraction between nanotubes [8], [15]–[17]. However, when surfactants are present, they adsorb onto the carbon nanotubes and form a highly repulsive structure able to overcome the strong attraction between nanotubes. This repulsion keeps the individual carbon nanotubes more isolated [18]–[22]. The diameter range provided by the supplier for the individual carbon nanotubes used is 1.2 – 1.7 nm, while the length range is 0.3 – 5.0 μm (Nanointegris).

It has previously been demonstrated that the diameter range of deposited single-walled carbon nanotubes can be modelled via a normal or Gaussian distribution [23]–[25]. However, when we directly extract and bin the height profiles from the $2.5 \mu\text{m} \times 2.5 \mu\text{m}$ AFM images, plotted in black in Figure 2.1, we obtain histograms which do not follow a normal distribution. One reason for this result is the surface roughness of the silicon dioxide substrate. The carbon nanotubes do not lie perfectly level on a perfectly level silicon oxide substrate. In practice, both the SiO_2 substrate and the surface of the carbon nanotubes both have a degree of roughness. To find the contribution of surface roughness to the height profile histogram corresponding to each network deposition method, silicon dioxide substrates were modified using the same processes as in Figure 2.1 but without carbon nanotubes present in the solutions used. $2.5 \mu\text{m} \times 2.5 \mu\text{m}$ AFM images of the modified surfaces are shown in Figure 2.2.

In Figure 2.2, we see that each substrate surface has a roughness that follows a normal distribution with some degree of skewness. Figure 2.2b and Figure 2.2d are negatively skewed distributions. The fitted skew-normal distribution in Figure 2.2b has a skew parameter α (or shape parameter) of -3.2, a location parameter ξ of 2.2 nm and a scale parameter ω of 0.5 nm, while in Figure 2.2d $\alpha = -2.2$, $\xi = 2.2$ nm and $\omega = 0.5$ nm. ξ and ω correspond to the mean and standard deviation of the skew-free normal distribution when α is set equal to zero [26]. The close correspondence between ξ and ω for these distributions but not α implies that the skewness is a variable imaging or processing artifact rather than a physical property of the surface. Without distortion, the roughness of a clean SiO_2 surface should follow a normal distribution [27].

2.2. Carbon Nanotube Network Morphology and Composition

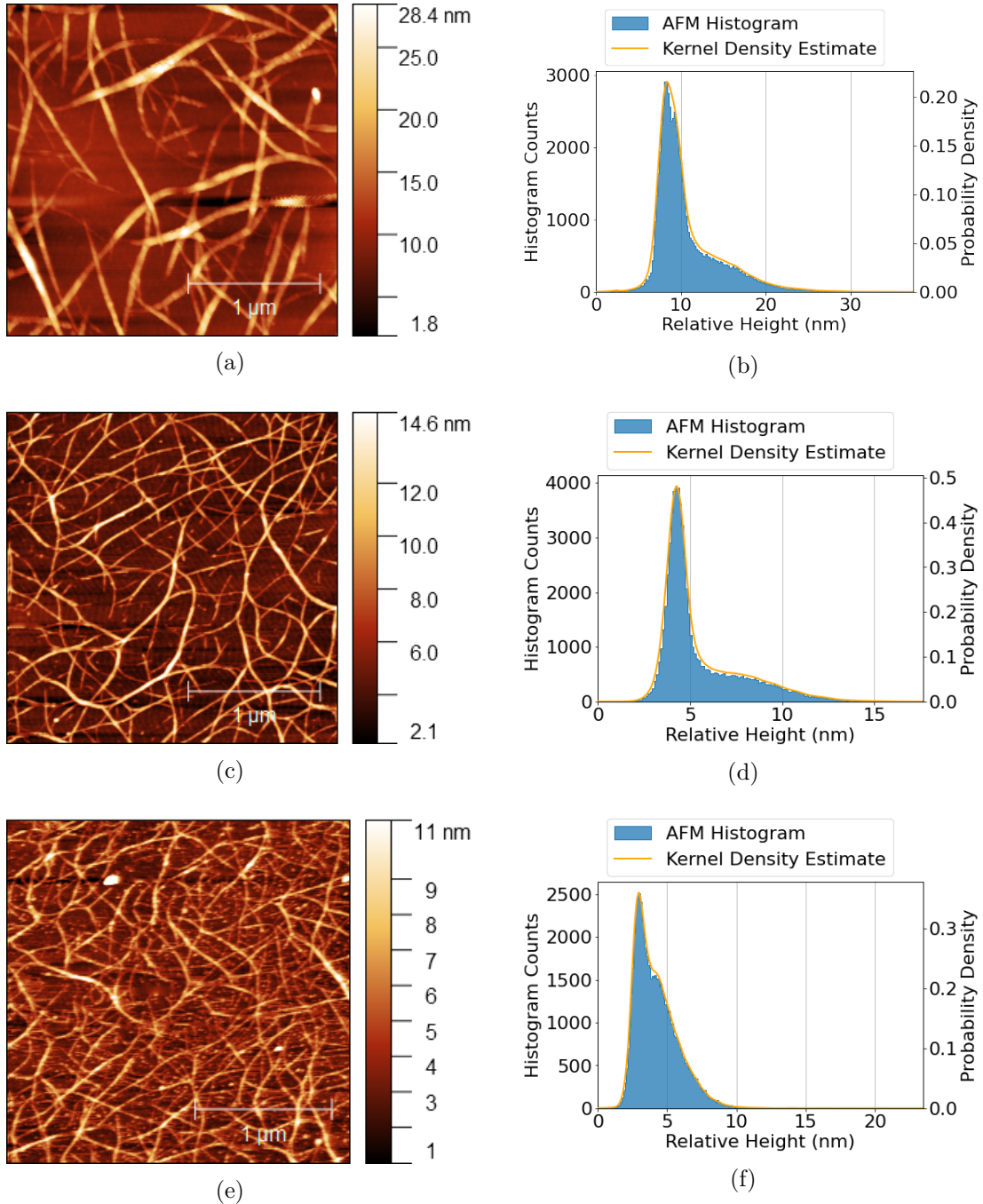


Figure 2.1.: $2.5 \mu\text{m} \times 2.5 \mu\text{m}$ atomic force microscope (AFM) images of carbon nanotube films deposited using various methods, shown side-by-side with histogram height distributions and kernel density estimate (KDE) plots corresponding to each image. The network shown in (a) with height distribution shown in (b) was deposited in solvent, the network shown in (c) with height distribution shown in (d) was dropcast in surfactant, and the network shown in (e) with height distribution shown in (f) was dropcast in surfactant with steam present.

2. Characteristics of Pristine Carbon Nanotube & Graphene Field Effect Transistors

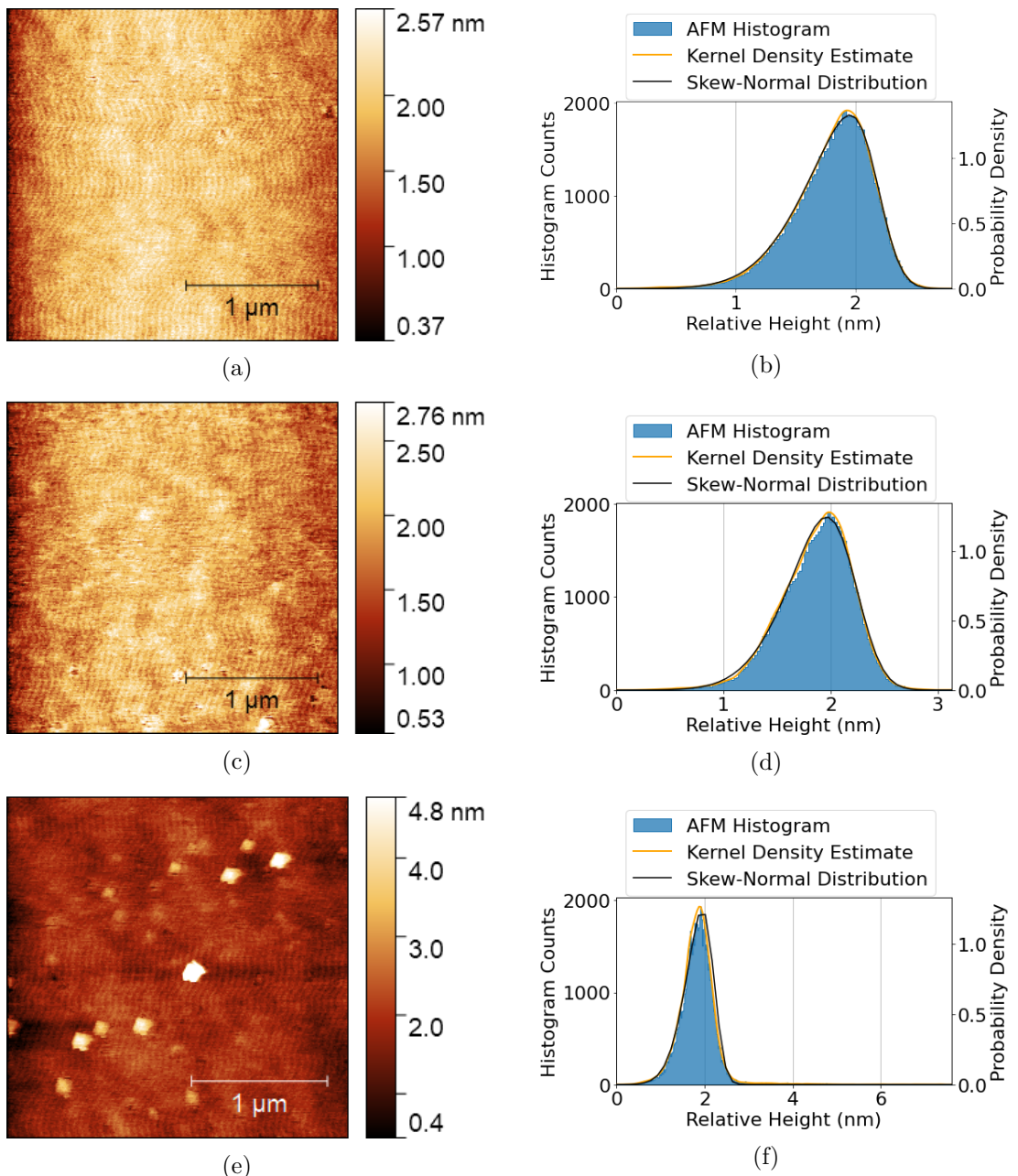


Figure 2.2.: $2.5 \mu\text{m} \times 2.5 \mu\text{m}$ atomic force microscope (AFM) images of silicon dioxide substrates alongside histogram height distributions and KDE plots corresponding to each image. The substrate in (a) and (b) was exposed to solvent, the substrate in (c) and (d) was exposed to surfactant, and the substrate in (e) and (f) was exposed to surfactant with steam present.

2.2. Carbon Nanotube Network Morphology and Composition

However, Figure 2.2f has a pronounced positive skew with a long tail. The tail appears to result from the contribution of residual surfactant aggregates to surface morphology, observed in Figure 2.2e and recently discussed elsewhere in the literature [25], [28]. Attempting to fit a skew-normal distribution to this histogram fails when all three variables are allowed to vary due to the presence of the tail. Instead, we fix ξ and ω at 2.2 nm and 0.5 nm respectively to mimic the silicon dioxide distributions previously obtained, and only α is allowed to vary during the fitting process. The result is shown in Figure 2.2f. The fitted distribution has an α of -2.4. The distribution closely fits the negative tail of the histogram, but deviates slightly from the positive tail due to the presence of surfactant. Since this deviation is small, the quality of the fit is still reasonably high, with an R-squared value of 0.98. Surfactant contamination could have negative effects on both sensitivity of carbon nanotubes and also could damage attached biological elements.

Using the morphology analysis technique outlined by Vobornik *et al.* [25], we collected five successive diameter measurements of 30 carbon nanotube bundles using Gwyddion. Measurements were not taken at bundle junctions. A height threshold ‘mask’ was defined in Gwyddion to determine average substrate height, as shown in Figure 2.3a. This background value was subtracted from our diameter measurements to determine the actual bundle height. The means of the solvent-deposited, surfactant-deposited and steam-assisted surfactant-deposited bundle diameter histograms are 8.8 ± 4.0 nm, 4.2 ± 1.8 nm and 3.3 ± 1.0 nm respectively. We see that an increased maximum feature height leads to an increased mean background height, and by examining the AFM images in Figure 2.1 we see that this may be due to deep artifacts on the surface of the substrate in the vicinity of large features. The average of the five height-adjusted values for each carbon nanotube bundle was then calculated, and these 30 averages were sorted into six equal-sized bins. The binned bundle diameter measurements, alongside estimated probability density, are shown in Figure 2.3.

We notice from Figure 2.3 that each histogram appears to follow a positively skewed normal distribution, different to the skew-free normal distribution we expect from previous works [23]–[25]. The skew is likely another artifact from imaging the network with the atomic force microscope. The force of the atomic force microscope tip is known to cause larger bundles to undergo some degree of compression, and the resulting systematic underestimation of their height may be responsible for the distribution skewness [25]. The fitted skew-normal distribution in Figure 2.3b has $\alpha = 2.7$, $\xi = 4.3$ nm, $\omega = 5.9$ nm, the distribution in Figure 2.3c has $\alpha = 2.4$, $\xi = 2.2$ nm, $\omega = 2.6$ nm, and the distribution in Figure 2.3d has $\alpha = 3.6$, $\xi = 2.2$ nm and $\omega = 1.5$ nm. We notice that the probability density for the carbon nanotube bundle histogram drops to approximately zero at or before 0 nm, as is physically appropriate.

2. Characteristics of Pristine Carbon Nanotube & Graphene Field Effect Transistors

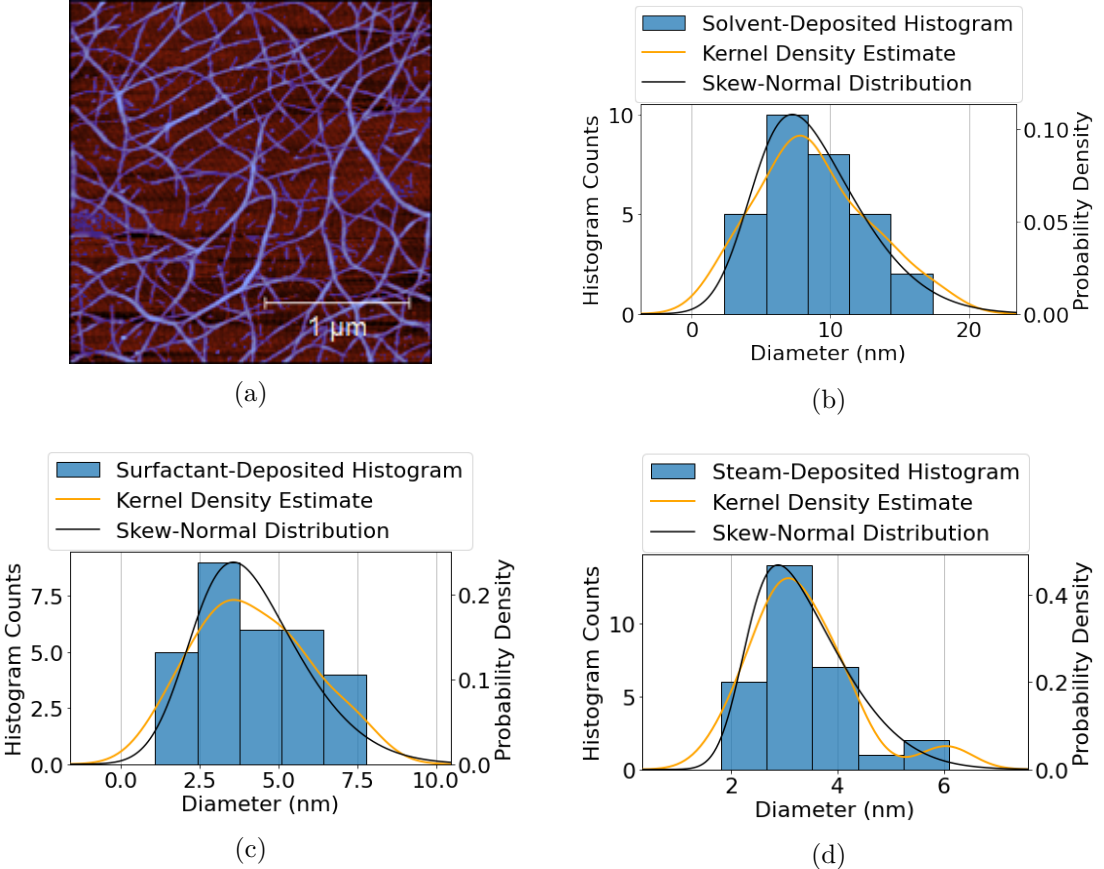


Figure 2.3.: An masked AFM image is shown in (a), where the masked carbon nanotube bundles are shaded blue. The mask sets a height threshold so that masked features are excluded from the height dataset. Histogram height distributions with corresponding KDE plots collected via the morphology analysis method outlined by Vobornik *et al.* [25] are shown in (b)-(d). The substrate in (b) was exposed to solvent, the substrate in (c) was exposed to surfactant, and the substrate in (d) was exposed to surfactant with steam present.

2.2. Carbon Nanotube Network Morphology and Composition

Table 2.2.: The mean of histogram distributions for carbon nanotube films deposited using various methods, alongside estimates for the number of nanotubes present per mean bundle and the estimated proportion of multi-tubed bundles present across the network.

	Mean Bundle Diameter (nm)	Tubes per Average Bundle	% Multi-Tube Bundles
Solvent deposited	8.8 ± 4.0	28	> 96%
Surfactant deposited	4.2 ± 1.8	5	> 75%
Surfactant deposited with steam	3.3 ± 1.0	3	> 65%

Table 2.1.: The first eight optimised ratios of 2D packed circle diameter to encompassing circle diameter, given to 3 s.f. (encompassing circle diameter = d , number of packed circles = n , approximate packed circle diameter = d_n).

n	2	3	4	5	6	7	8	9
d/d_n	2.00	2.15	2.41	2.70	3.00	3.00	3.30	3.61

If we model carbon nanotube bundles as cylinders, and we assume the component nanotubes follow 2D packing and are of equal diameter, we can state the mean bundle size for each deposition type in terms of number of nanotubes n [8], [29], [30]. Table 2.1 shows the relationship between the diameter of a bundle and the constituent diameters of up to nine 2D packed carbon nanotubes within that bundle. Assuming an average carbon nanotube diameter of 1.45 nm, we can use the d/d_n packing ratios to obtain an estimate of the number of nanotubes in the mean bundle size for each deposition [30]. These estimates are shown in Table 2.2. Also shown in Table 2.2 is an estimate of the ratio of single- to multi-tube bundles for each deposition. This estimate was obtained by taking the integral of each distribution with a lower bound of 2.9 nm, the minimum multi-tube bundle size for 1.45 nm diameter nanotubes. As the area under the curve represents the probability a bundle will have a particular diameter, this integral should give a good estimate of the relative proportion of multi-tube bundles. Table 2.2 should be interpreted as lower-limit estimates of the size and relative proportion of bundles, recalling that the distribution skewness indicates underestimation of the true bundle height.

Both the carbon nanotube bundle diameter mean and standard deviation are small for surfactant-deposited films when compared to the mean and standard deviation of solvent-deposited films. However, despite the presence of surfactant, it is apparent both from Figure 2.1 and Table 2.2 that not all surfactant-dispersed carbon nanotubes are deposited individually. Bundling may occur during the process of deposition onto the

2. Characteristics of Pristine Carbon Nanotube & Graphene Field Effect Transistors

substrate, which could disrupt the repulsive forces from the surfactant coating and allow attractive forces to temporarily dominate. It is possible that the bundling of surfactant-dispersed carbon nanotubes is a consequence of dynamics introduced by the coffee-ring effect [31], [32]. The coffee-ring effect refers to a build-up of dispersed solid forming around the edges of a dispersion evaporating on a surface. This process occurs due to the dispersion edges being fixed by surface forces, leading to capillary flow outwards to replace liquid evaporating at the edges, bringing solid material along with it. The presence of vapour is known to disrupt this capillary effect [33], which may explain why mean bundle diameter is lower for the films deposited in surfactant with steam present relative to films deposited in surfactant without steam.

From this discussion, we can conclude that the histograms shown in Figure 2.1 are linear combinations of skewed normal distributions corresponding to both the substrate surface, with a negative skew, and the carbon nanotube bundles, with a positive skew. X and Y junctions between overlapping nanotubes may also form a similarly skewed normal distribution as part of the full histogram [8]. The complete linear combination could be modelled mathematically in order to rapidly extract key parameters from atomic force microscope images [34], but implementing this approach is outside of the scope of this thesis. The prevalence of carbon nanotube bundling on the surface is lowered by the presence of surfactant during deposition. Introducing steam when depositing with surfactant lowers bundling even further, but also leads to residual surfactant pooling and attaching to the substrate surface. These results may both be explained by the presence of steam enabling surfactant to follow carbon nanotubes to the substrate surface, which keeps them from bundling during the attachment process. The unwanted persistence of surfactant means that higher temperature vacuum annealing may be required for robust biosensors [35].

2.2.2. Raman Spectroscopy

Raman spectroscopy was also used to analyse and compare the deposited carbon nanotube networks. Raman spectra were collected from a solvent-deposited carbon nanotube film and a steam-assisted surfactant-deposited film, both on silicon dioxide, in the manner described in Section 1.6. These spectra were then processed using the Python script mentioned in Section A.3. For each location, spectra over two wavenumber ranges were collected. A peak corresponding to the silicon dioxide substrate, found in the range between 100 cm^{-1} and 650 cm^{-1} , was used as a reference peak for the normalisation of intensities across the range between 1300 cm^{-1} and 1650 cm^{-1} . These normalised spectra are shown in Figure 2.4. In all spectra, a D-band comprising a single D-peak is observed at $\sim 1320\text{ cm}^{-1}$, and a G-band comprising two G-peaks, G^- and G^+ is observed between $\sim 1525\text{ cm}^{-1}$ and $\sim 1650\text{ cm}^{-1}$. These features are characteristic of networks of semiconducting carbon nanotubes [36], [37].

Closer inspection of the D peak and G peaks can give us important information about network composition. G^- is a minor peak found at $\sim 1570\text{ cm}^{-1}$, while G^+ is a larger

2.2. Carbon Nanotube Network Morphology and Composition

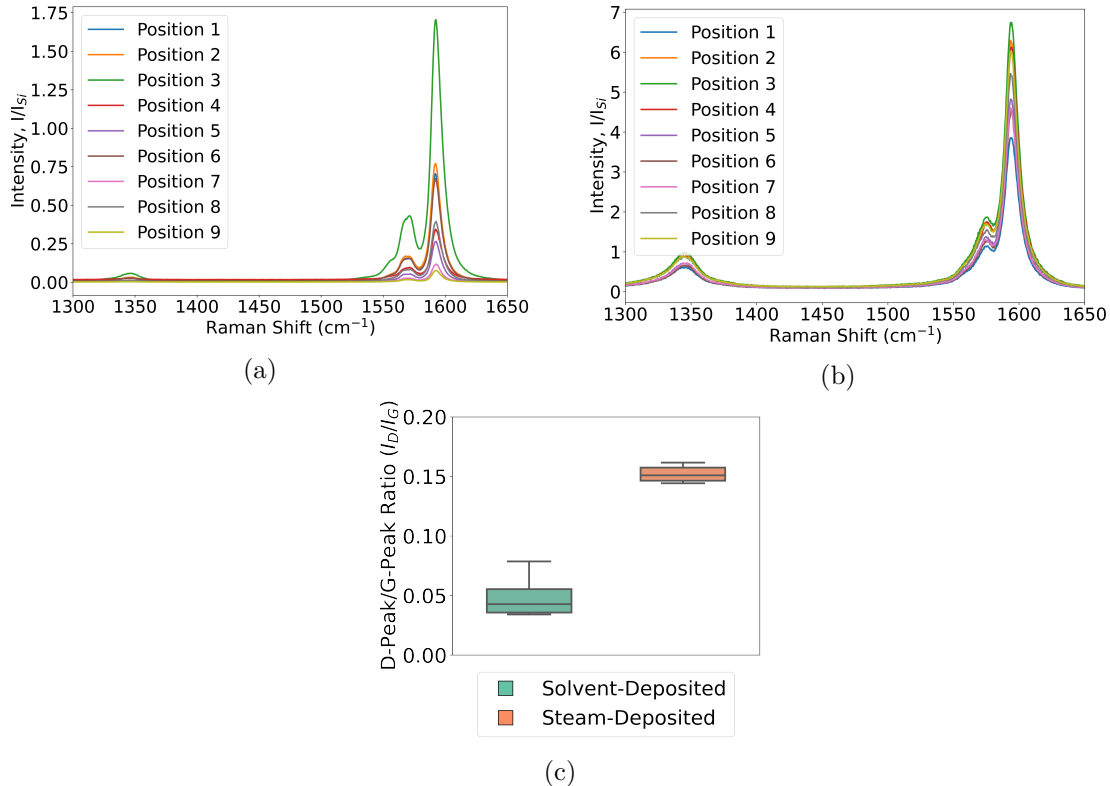


Figure 2.4.: A series of nine Raman spectra at different locations across a $10 \mu\text{m} \times 50 \mu\text{m}$ carbon nanotube film region, spaced at least $10 \mu\text{m}$ apart, with (a) showing spectra from a film deposited in solvent and (b) showing spectra from a film deposited in surfactant with steam present. (c) shows the spread of the D-peak/G⁺-peak spectral ratios corresponding to each film.

2. Characteristics of Pristine Carbon Nanotube & Graphene Field Effect Transistors

feature at $\sim 1590 \text{ cm}^{-1}$. The G^+ feature describes the in-plane vibration of carbon bonds along the length of the carbon nanotubes, while the G^- feature describes the in-plane vibration of bonds about the nanotube circumference [37], [38]. The splitting between the wavenumber location of the G^- and G^+ local maxima is lower in Figure 2.4b than in Figure 2.4a, indicating more metallic nanotubes are present in the surfactant-deposited network [38]. The D-peak gives an indication of the defects present in the carbon nanotube atomic structure [37], [38]. We notice that the size of the normalised D-peak is much lower in Figure 2.4a than in Figure 2.4b, indicating the solvent deposition process introduces less defects to the carbon nanotubes than surfactant-mediated deposition.

It is also possible to compare the relative magnitude of the D-peak and G^+ -peak intensity to quantify carbon nanotube structural disorder, which disrupts in-plane lattice vibration [36], [37]. Figure 2.4c gives a summary of the ratios between the D-peak and G^+ -peak across all nine positions for the solvent-deposited and surfactant-deposited film. It is immediately observed that I_D/I_G is significantly larger for the steam-assisted, surfactant-deposited films than for the solvent-deposited films. This is a further indication of the presence of defects across the steam-deposited network. These defects are likely introduced through the introduction of charge impurities by surfactant aggregates present around the carbon nanotubes [28]. However, we also notice that the range of values for the I_D/I_G ratio is lower for the steam-deposited network. This spatially homogeneous vibrational behaviour implies the steam-deposited network is more evenly distributed than the solvent-deposited network, which matches the discussion in Section 2.2.

2.3. Electrical Characteristics of Pristine Devices

2.3.1. Carbon Nanotube Network Devices

Each carbon nanotube device fabricated was electrically characterised as described in Section 1.7, and electrical data was analysed using the Python code discussed in Section A.4. Devices with a 100 nm or 300 nm SiO_2 layer were used for liquid gated measurements, and devices with a 100 nm SiO_2 layer were used for backgated measurements. Figure 2.5 displays multi-channel measurements of representative devices fabricated as described in Chapter 1. To ensure a consistent comparison, each device here was encapsulated with AZ® 1518 encapsulation before measurements were taken. The channels which did not exhibit reliable transistor characteristics are not shown. These ‘non-working’ channels were either shorted, due to metal remaining on the channel after lift-off, or were very low current, due to a very sparse carbon nanotube network. Devices shown here with a solvent-deposited carbon nanotube network were fabricated prior to Jan 2022; devices with a surfactant-deposited network without steam present were fabricated prior to Jun 2021; devices with a surfactant-deposited network without steam were fabricated prior to Sep 2022.

2.3. Electrical Characteristics of Pristine Devices

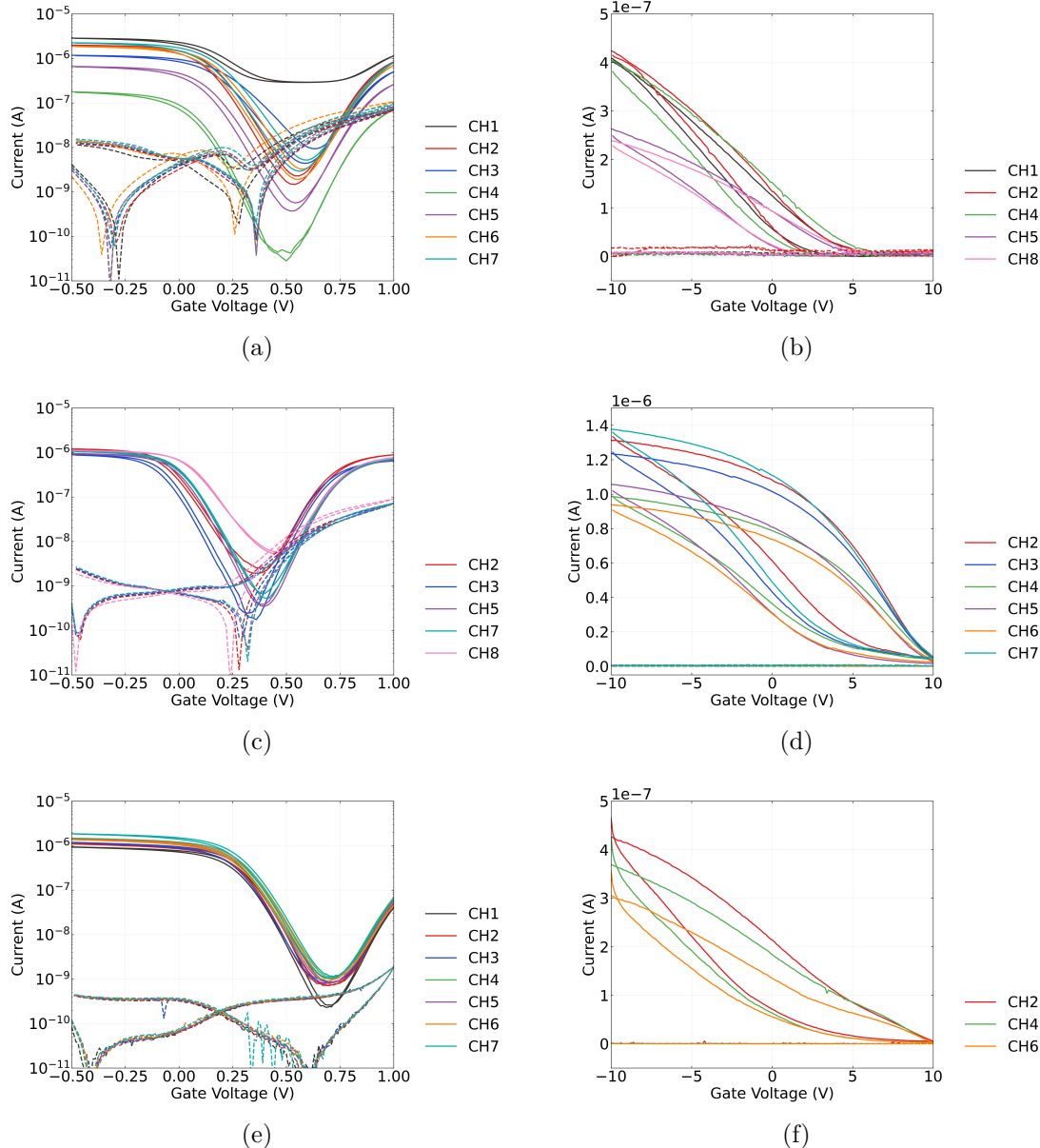


Figure 2.5.: Liquid-gated (left) and back-gated (right) transfer characteristics of AZ® 1518 encapsulated field-effect transistors, where the film was deposited with solvent in (a) and (b), deposited with surfactant in (c) and (d), and deposited with surfactant in the presence of steam in (e) and (f). A step size of 100 mV was used for the backgated sweeps in (a), (c) and (e), while a step size of 20 mV was used for the liquid-gated sweeps in (b), (d) and (f). Gate current (leakage current) is shown with a dashed line. The source-drain voltage used for all sweeps was $V_{ds} = 100\text{mV}$, and 1XPBS was used as the buffer for the liquid-gated measurements here.

2. Characteristics of Pristine Carbon Nanotube & Graphene Field Effect Transistors

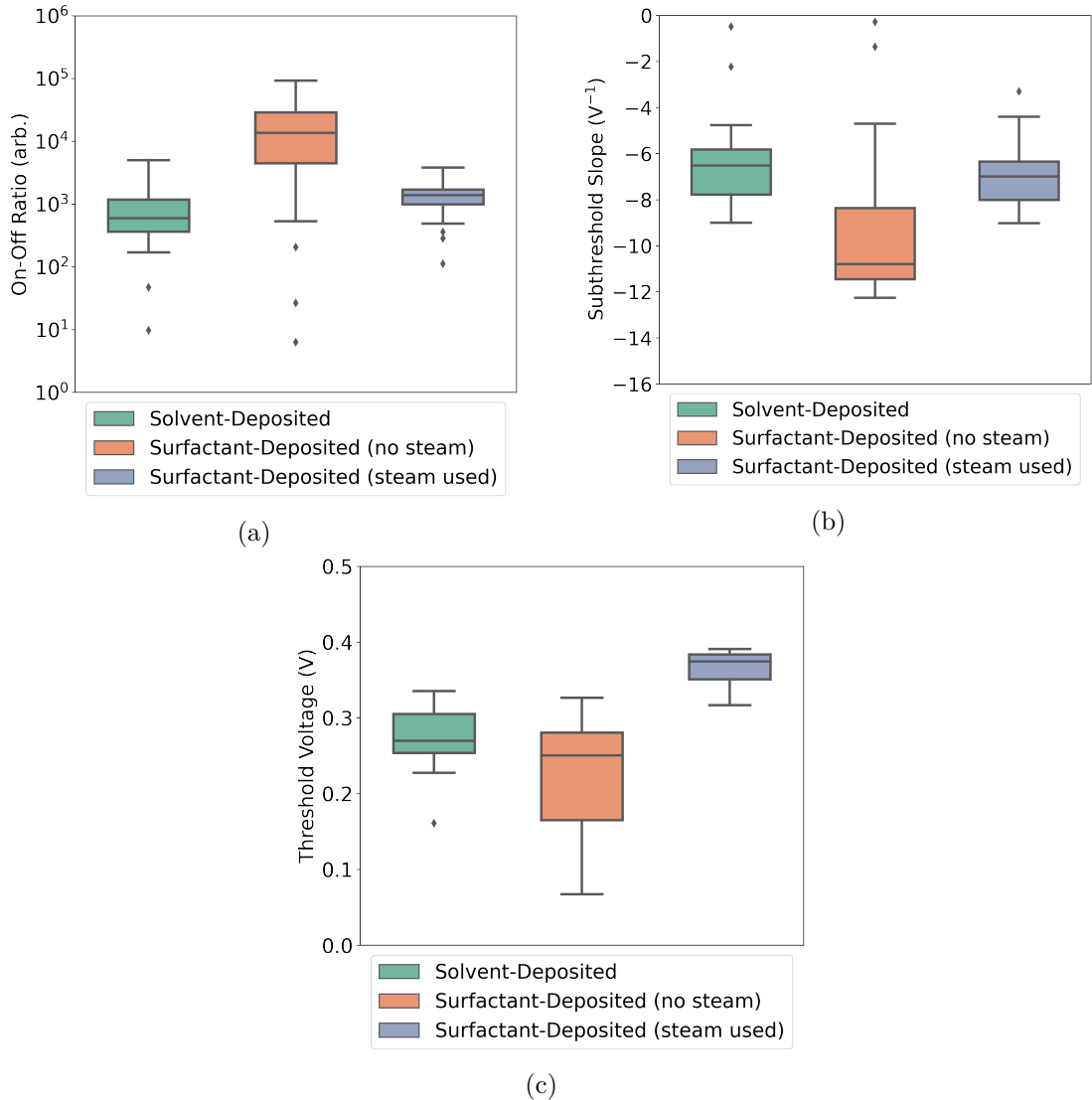


Figure 2.6.: These boxplots illustrate the statistical distribution of (a) the on-off ratio, (b) the subthreshold slope, and (c) the threshold voltage of AZ® 1518 encapsulated liquid-gated transistor channels corresponding to each type of carbon nanotube film deposition. For each deposition type, electrical characteristics were taken of 21 channels of at least three separate devices. The boxes indicate the 25th and 75th percentile of the distribution.

Liquid-Gated CNTFETs

The liquid-gated devices in Figure 2.5a, Figure 2.5c and Figure 2.5e each exhibited ambipolar characteristics, commonly observed in liquid-gated carbon nanotube network FETs [3], [8], [39]–[42]. When devices were appropriately configured, leakage current (shown by the dashed traces) did not exceed $\sim 1 \times 10^{-7}$ V across the forward and reverse sweep. The devices shown which used steam-deposited carbon nanotube films showed the least hysteresis. From Section 2.2.1, we know the mean diameter of the bundles in these films is about 0.9 nm less than the mean bundles in films deposited without steam present, and 5.5 nm less than those in films deposited in solvent. Hysteresis is known to scale roughly linearly with bundle diameter, due to trapped charge increasing as bundle density of states is increased [43]. Steam-deposited devices also showed significantly less channel-to-channel variation in electrical characteristics more generally. Channel 1 in Figure 2.5a has a much higher off-current than the other channels of the same device, which appears to be due to a uncommonly high proportion of metallic carbon nanotubes present in the network conduction pathways of this channel [44], [45].

A summary of key parameters of pristine liquid-gated devices is shown in Figure 2.6. The full dataset consists of three sets of 21 liquid-gated transfer characteristics of working channels, with each set corresponding to the use of a particular method of carbon nanotube network deposition in the device fabrication. Measurements from at least three devices are included in each set. Each entry in the summary corresponds to the average of the specific parameter in the forward and reverse sweep direction. When steam was used for surfactant deposition of films, the resulting devices showed highly consistent channel-to-channel electrical properties. As the carbon nanotube films on these devices are relatively dense, as seen in Figure 2.1e, we know that the network is well above the percolation threshold. As many carbon nanotube pathways connect across the channel in parallel, small variations in the network morphology have less of an impact on the overall channel behaviour [8]. We also see from Figure 2.3 and Table 2.2 that the range of bundle sizes is relatively low in the steam-deposited films used in these devices, meaning the electrical behaviour of dominant conduction pathways is more spatially consistent. The repeatable subthreshold regime behaviour between channels seen for steam-deposited devices is a desirable attribute for reliable real-time multiplexed biosensing [39], [40], [46].

Channels from surfactant-deposited film devices usually showed a larger on-off ratio and subthreshold slope than those from solvent-deposited devices. Decreasing the ratio of gate-sensitive semiconducting carbon nanotubes to metallic nanotubes tends to decrease the on-off ratio [8], [23], [44], [45]. Section 2.2.2 seems to indicate there are more metallic nanotubes present in the surfactant-deposited films than in the solvent-deposited films. However, percolating conduction pathways dominate device behaviour and nanotube pathways across the channel with a lower degree of bundling are less likely to contain metallic tubes [8]. Therefore, the larger on-off ratio for surfactant-deposited film devices is likely a result of their reduced nanotube bundle size and reduced bundle size variation

2. Characteristics of Pristine Carbon Nanotube & Graphene Field Effect Transistors

relative to other films, as discussed in Section 2.2. The larger subthreshold slope is likely due to increased mobility from a denser nanotube network in surfactant-deposited films [44], as seen in Figure 2.1e. A larger on-off ratio and subthreshold slope results in a larger change in conductance in response to changes in the transfer characteristic curve. Therefore, the larger on-off ratio and subthreshold slope of steam-deposited devices is desirable for improved sensor performance [39], [40], [46].

All channels characterised had a positive threshold voltage (V_{th}). The threshold voltage was largest and most consistent for steam-assisted surfactant-deposited films. The relatively high values of V_{th} which correspond to channel measurements from steam-assisted surfactant-deposited devices indicates increased *p*-doping of the network relative to networks deposited via alternative processes [8], [47], [48]. As seen from Figure 2.2e-f and Figure 2.4c, the steam deposition process leads to the presence of significant, persistent surfactant aggregates. It has been previously established that residual surfactant can *p*-dope carbon nanotubes, alongside enhancing *p*-doping from adsorbed oxygen and water [28], [35], [49]. The presence of residual surfactant may also explain the lowered subthreshold slope, and therefore mobility, of the steam-deposited devices relative to devices with films deposited in surfactant without steam. The analysis by Kane *et al.* shows that the thermal annealing at 150°C used in this work to remove residual surfactant is likely inadequate for this purpose. Oxidation of devices and vacuum annealing at high temperatures ($> 600^\circ \text{C}$) may be required for effective desorption of the persistent surfactant [35], [50]. Devices using films made using the alternative two methods have the advantage of not requiring careful treatment to remove surfactant.

Back-Gated CNTFETs

When characterising devices using the vapour delivery system chip carrier, the setup arrangement meant all measurements were taken using a backgate. From Figure 2.5b, Figure 2.5d and Figure 2.5f, we see backgated devices exhibited *p*-type transistor behaviour. Gate current leakage was negligible, as shown by the dashed line staying close to zero across the sweep. Significant hysteresis was observed. The hysteresis can be explained by the presence of defects or charge traps within and on the surface of the silicon dioxide and at interfaces between the silicon dioxide and carbon nanotubes [51]–[53]. The hysteresis observed was much greater than for the corresponding liquid-gated sweeps on the right. The devices fabricated with a solvent-based deposition were switched off at a lower voltage than the devices which used surfactant during deposition.

Transfer measurements were taken to determine whether backgated measurements could be taken of an unencapsulated device in the vapour sensor chamber with 1XPBS covering the channels. Figure 2.7 shows the behaviour of an unencapsulated backgated device with a 300 nm SiO₂ layer before and after being covered by 50 μL of 1XPBS (phosphate buffered saline). The on-off ratio and hysteresis of the channels increase significantly. The presence of water increases hysteresis through introducing charge traps at the silicon dioxide surface around the carbon nanotubes and at the surface of the nanotubes

2.3. Electrical Characteristics of Pristine Devices

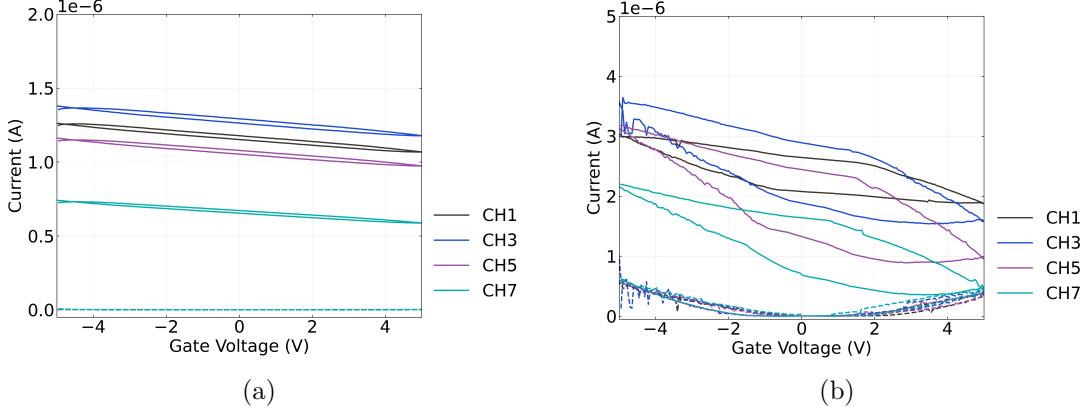


Figure 2.7.: Backgated transfer sweeps were taken of an single unencapsulated device with a 300 nm SiO_2 layer and steam assisted surfactant-deposited carbon nanotube network channels before and after being covered in $50\mu\text{L}$ 1XPBS electrolyte.

themselves [51], [53]–[55]. There is also a significant increase in current leakage to the backgate for larger applied voltages, despite the electrolyte having no visible physical contact with the silicon backgate or copper plane. This leakage current may simply be due to an increase in relative humidity around the device due to the presence of water [56]. As any variation in threshold voltage due to hysteresis and significant leakage current are undesirable for sensing procedures, this configuration was not used for vapour sensing purposes.

2.3.2. Graphene Devices

Graphene field-effect transistor devices were electrically characterised in the manner described in Section 1.7 and analysed using the Python code discussed in Section A.4.

Figure 2.8 shows the liquid-gated transfer characteristics of two graphene devices. These devices were fabricated prior to Jun 2021. Both devices exhibit the ambipolar characteristics typical of liquid-gated graphene devices [57]–[60]. As with the carbon nanotube network devices, leakage current remained below $\sim 1 \times 10^{-7}$ V across both the forward and reverse sweep. Hysteresis between the forward and reverse sweep is caused by trapping of charge within and on the surface of the SiO_2 dielectric [61]. The major Dirac point for these devices is slightly to the right of $V_{\text{Dirac}} \approx 0$ V, which indicates *p*-doping of the channel. This slight *p*-doping is likely a result of a adsorption of oxygen and water from the air and residue resist from photolithography [60], [62], [63].

Some devices exhibited a double-minima feature, indicating the presence of two Dirac points. This effect arises due to doping of graphene by the metal contacts. In shorter length channels, metal doping affects the entire channel length, leading to a consistent

2. Characteristics of Pristine Carbon Nanotube & Graphene Field Effect Transistors

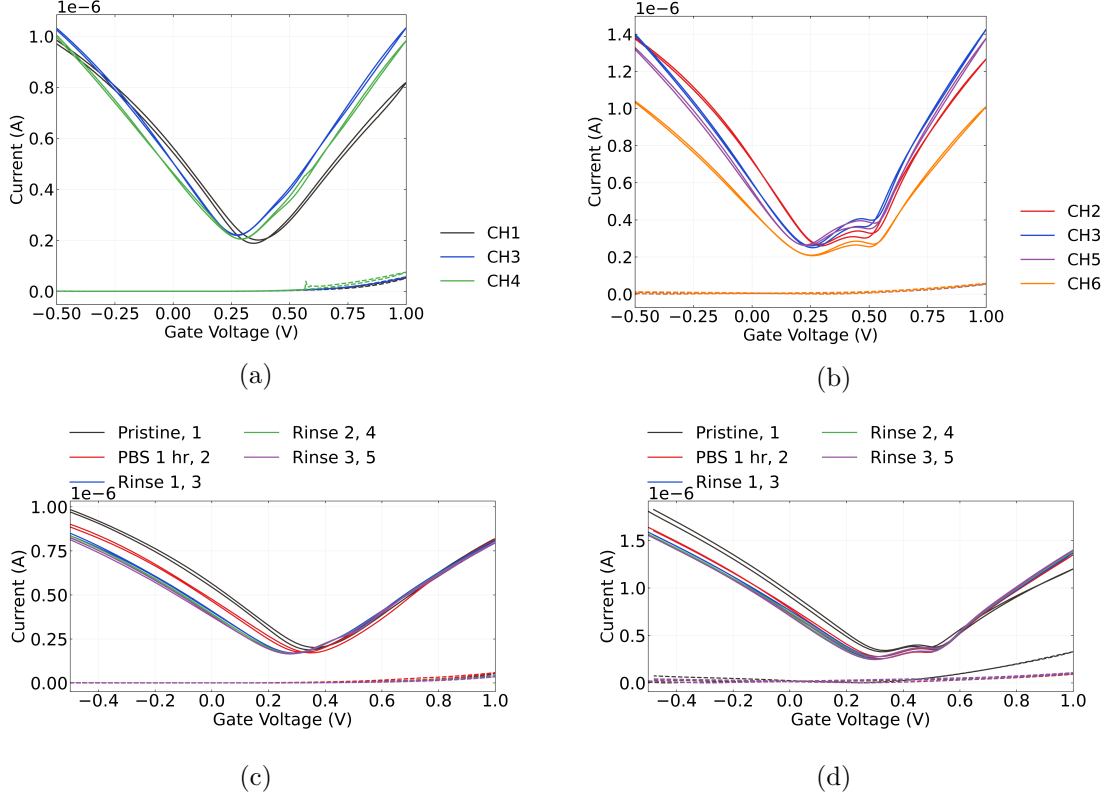


Figure 2.8.: These figures show liquid-gated transfer characteristics of channels from two AZ® 1518 encapsulated graphene devices. The characteristics of working device channels upon initial exposure to 1XPBS are shown in (a) and (b). The transfer characteristics of channel 1 in (a) and channel 5 in (b) after various degrees of exposure to 1XPBS are shown in (c) and (d) respectively, with each transfer sweep numbered in the order the sweeps were taken. The dashed lines correspond to measurements of gate leakage current.

2.4. Real-Time Salt Concentration Sensing with Phosphate Buffered Saline

Table 2.3.: Average on-off ratio and major Dirac point voltage for AZ® 1518 encapsulated liquid-gated graphene transistor channels at various stages of exposure to 1XPBS. Electrical characteristics were taken of 6 channels total, three channels from each of two devices.

	1XPBS: Initial	1XPBS: After 1 hr	1XPBS: Rinse
On-Off Ratio (arb.)	5.1 ± 0.3	5.0 ± 0.7	5.0 ± 0.6
Dirac Point Voltage (V)	0.28 ± 0.04	0.31 ± 0.03	0.28 ± 0.02

Fermi level and a single Dirac point. However, for longer channel lengths like ours, the doping effect from metal contact no longer reaches the entire channel, leading to a difference in Fermi level between the graphene in the channel and graphene under the metal contact. The difference in Fermi levels results in the presence of a second Dirac point [61], [64], [65]. The global minimum of the transfer characteristic can be referred to as the ‘major’ Dirac point.

Figure 2.8 also shows the effect of 1XPBS on the graphene channels. The channels were measured on exposure to 1XPBS, after exposure to 1XPBS for one hour, and after the device surface was rinsed and 1XPBS was replaced in the well one time, two times and three times successively. A slight negative shift of the major Dirac point was observed. This effect is possibly a result of gate bias stress, where successive transfer sweeps introduce charge traps to the graphene layer and alters the current level at a given gate voltage [66], [67]. Alternatively, Kireev *et al.* found that a series of liquid-gated sweeps also reduced the size of the second Dirac point, and suggested that it indicated the gate current was removing atmospheric contaminants from the graphene surface via current annealing [60]. This could be explained as the removal of contaminants causing improved contact between the metal and graphene surface, and thus increasing metal doping and consistency of the Fermi level across the channel. If the contaminants removed are *p*-dopants, then this effect could also explain the negative shift of the major Dirac point.

Table 2.3 shows the on-off ratio and major Dirac point voltage of the graphene devices. Apart from the previously-mentioned slight negative shift of the major Dirac point, these values were highly consistent before and after exposure to 1XPBS.

2.4. Real-Time Salt Concentration Sensing with Phosphate Buffered Saline

2.4.1. Control Series and Baseline Drift

2. Characteristics of Pristine Carbon Nanotube & Graphene Field Effect Transistors

Table 2.4.: The threshold voltages V_{th} of each working channel of a steam-deposited device, and the difference between each V_{th} and the mean device threshold voltage $V_{th,mean}$.

Channels	CH1	CH2	CH3	CH5	CH6	CH7
Threshold voltage (mV)	160	150	130	140	180	140
Relative to mean (mV)	10	0	-20	-10	30	-10

To verify the sensitivity of the fabricated field-effect transistors and therefore verify their suitability for sensing, control measurements replicating a typical sensing experiment were taken before functionalising the device channels. This involved first ensuring the device showed no response to 1XPBS, a sequence referred to here as the ‘PBS control series’. The PDMS well contained 80 μL 1X PBS at 0 s. The PBS control series ran over the first 1800 s, with 20 μL phosphate buffer saline (1XPBS) additions at 100 s, 200 s and 300 s, and 20 μL subtractions at 400 s, 500 s and 600 s. The device was left untouched over the next 1200 s to allow the current level to settle. The gate voltage was held at $V_g = 0 \text{ V}$.

Figure 2.9a shows the transfer sweeps of the six working channels of a steam-assisted surfactant-deposited carbon nanotube field-effect transistor encapsulated with AZ® 1518, fabricated in Mar 2023 and measured using the PXIE. The central ‘negative current’ feature in the transfer characteristics of channels 1 and 7 is due to unphysical measurements which come from equipment error and can be treated as zero current passing through the channel. The threshold voltages of the channels are shown in Table 2.4. Table 2.4 also shows the difference between the threshold voltage of each channel and the mean threshold voltage of the device. The mean threshold voltage was $V_{th} = 150 \pm 20 \text{ mV}$. As discussed previously, the electrical characteristics are highly consistent between the channels due to the film deposition method used.

Figure 2.9b shows the PBS control series corresponding to each device channel alongside gate current. In both series, there is no clear stepwise response to any addition or subtraction of 1XPBS. Gate leakage current remains negligible across the entire control series, with no change in response to 1XPBS additions. We see that the current has a period of faster decay followed by slower baseline drift, similar to observations by Lin *et al.* and more recently Noyce *et al.* for parallel arrangements of single carbon nanotubes in air or vacuum [67], [68]. This effect results from changes in the occupancy of charge traps in and around the substrate and carbon nanotubes. The magnitude of baseline drift is lower for our devices than for those characterised by Noyce *et al.*, which may be a result of numerous device and setup differences which affect the presence of charge traps. These differences include liquid-gating instead of back-gated, the use of a network of carbon nanotubes instead of single nanotubes, a different channel length, the use of a 300 nm instead of 90 nm SiO_2 layer, and the use of an asymmetric, liquid-gated transfer

2.4. Real-Time Salt Concentration Sensing with Phosphate Buffered Saline

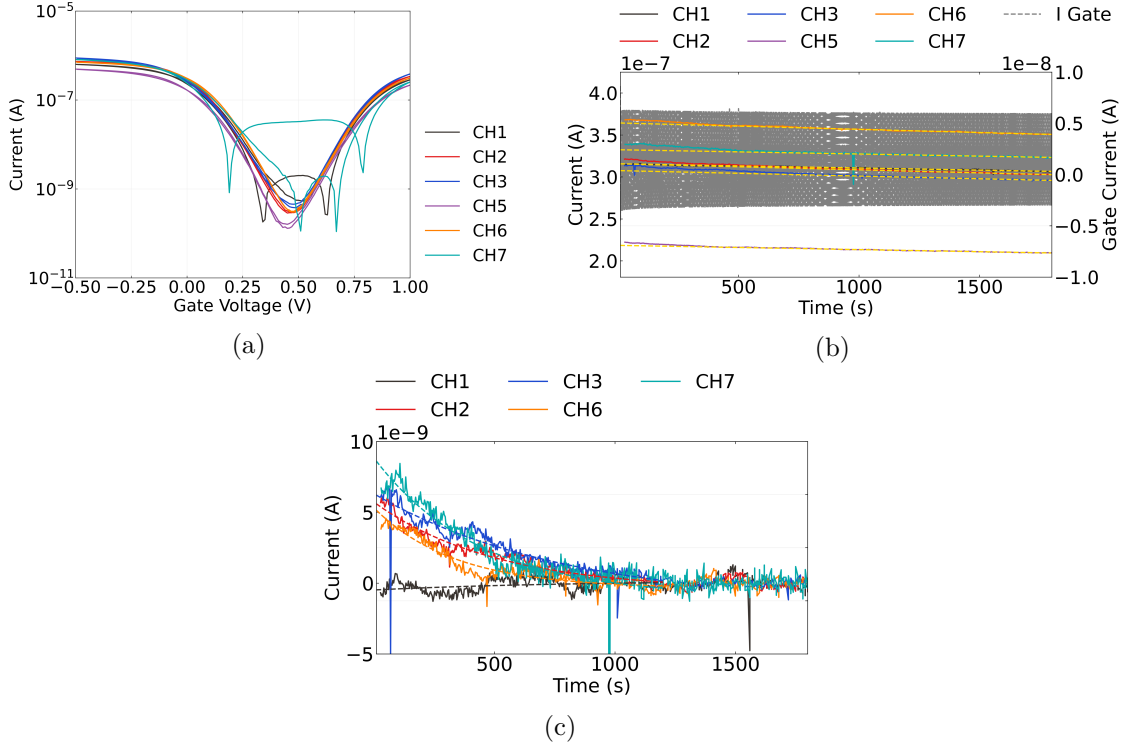


Figure 2.9.: The transfer characteristics in (a) were taken of the steam-deposited carbon nanotube field-effect transistor used here for an example of salt concentration sensing. The absolute values of measurements are shown, so that negative values resulting from measurement error can be visualised. Linear fits to the PBS control series from each channel from 1200 s onwards are shown in (b), while exponential fits to the PBScontrol series from 0 – 1200 with the linear fit subtracted are shown in (c). No significant response to PBS additions are seen at any of the addition times from 100 s - 600 s.

2. Characteristics of Pristine Carbon Nanotube & Graphene Field Effect Transistors

sweep over a shorter voltage range to characterise devices before each control series was measured [67].

Table 2.5.: The coefficients of linear fits to the PBS control series of each channel between 1200 – 1800 s, where m is the gradient and b is the constant term.

Channels	CH1	CH2	CH3	CH5	CH6	CH7
m (pA/s)	-5.1±0.2	-7.2±0.1	-6.5±0.1	-5.0±0.1	-7.6±0.1	-5.1±0.2
b (μ A)	0.316	0.316	0.308	0.218	0.364	0.332

Table 2.6.: The coefficients of exponential fits to the PBS control series of each channel between 0 – 1200 s, after the linear fit has been subtracted, where a is the gradient and τ is the time constant.

Channels	CH1	CH2	CH3	CH6	CH7
a (nA)	-0.66 ± 0.26	6.21 ± 0.09	7.84 ± 0.41	5.67 ± 0.11	9.82 ± 0.47
τ (s)	800 ± 750	500 ± 30	790 ± 100	330 ± 20	440 ± 70

As a first approximation to the longer time constant exponentials discussed by Noyce *et al.*, linear fits were performed on each PBS control series from 1200 – 1800 s. These linear fits are shown by the dashed yellow lines in Figure 2.9b. The parameters from each fit in Figure 2.9b are shown in Table 2.5, where $I = mt + b$. The fits for channels 1, 5 and 7 are all in parallel within error. We also notice that the gradient of fits in Figure 2.9b is reasonably consistent across all channels, with gradient values all falling within a 2.6 pA/s range. When the long-term linear fits were subtracted from the raw data, the remaining dataset followed a exponential decay trend for both control series. Figure 2.9c shows exponential fits to the remaining curve from 0 – 1200 s, which was successful for all channels except channel 5. The parameters from each fit are shown in Table 2.6, where $I = a \exp(-t/\tau)$. The exponential fits had characteristic time constants ranging between 300 – 800 s, indicating that 1800 s is a sufficient length of time for this short-term baseline drift to completely decay to zero. The exponential term for channel 1 is close to linear, indicating the channel has low net trapped charge. It is unclear why the behaviour of this channel is significantly different from the others.

From this analysis it appears that the baseline drift for the liquid-gated carbon nanotube devices can be accurately approximated as a combination of a exponential and linear term. The lack of response to 1XPBS at any of the six PBS addition and removal times gives us confidence that this is a stable baseline which can be used for reliable chemical sensing. Furthermore, after ~ 800 s the baseline drift can be reasonably approximated as linear, with a small gradient of less than -10 pA/s. The slow change of current means

2.4. Real-Time Salt Concentration Sensing with Phosphate Buffered Saline

Table 2.7.: This table shows the times at which 20 μL additions were made to the PDMS well, with 300 s between each addition. The concentration in the well after each addition and the change in concentration after each addition are also shown. The well contained 80 μL of 1X PBS at 1800 s.

	1X PBS Addition			DI Water Additions		
Time (s)	2100	2400	2700	3000	3300	3600
Final PBS volume (μL)	100	120	140	160	180	200
Final PBS concentration	1X	0.83X	0.71X	0.63X	0.56X	0.50X
Δ PBS concentration	0	-0.17X	-0.12X	-0.09X	-0.07X	-0.06X

that it becomes easier to distinguish responses due to analyte addition. We can therefore conclude that the 1800 s length of the PBS control series is appropriate for minimising baseline drift for more reliable sensing.

2.4.2. Sensing Series

A salt concentration sensing series were performed from 1800 s onwards, directly after the PBS control series. The responses to successive dilutions of the liquid-gate electrolyte were recorded to confirm the fabricated devices were sensitive to small environmental changes in their pristine state, to check for spurious signals, and to ensure gate current leakage or other confounding factors were not contributing to sensing responses. The PDMS well contained 80 μL 1X PBS at 1800 s. During the series, successive additions of deionised water were made to reduce the concentration of PBS in the well. An initial 1X PBS addition was performed at 2100s, to confirm no changes occurred during the PBS control series that would interfere with sensing. All additions to the well in the sensing series and resulting changes to the PBS concentration in the well are shown in Table 2.7.

Figure 2.10a shows a multiplexed salt concentration sensing series from the channels of a single AZ® 1518 encapsulated device, measured with the NI-PXIe. The gate voltage used was 0 V, which meant current measurements were well above the magnitude of the subthreshold device current. Gate current measurements did not exceed 1 nA for the SU8 encapsulated devices, and did not exceed 10 nA for the AZ® 1518 devices. At each of the deionised water addition times, the current traces for at least two out of six channels showed a sharp, transient increase in current followed by a return to an increased baseline. It is well established that changing the salt concentration of the liquid gate has an electrostatic gating effect on the carbon nanotubes or graphene, and changes the transfer characteristics of the channel. This shift in transfer characteristic means we observe a realtime signal response to each addition [40], [58], [60].

Using the data in Table 2.5, we can subtract the linear term approximating baseline drift (mt) for each channel from the data in Figure 2.10a to account for the downward

2. Characteristics of Pristine Carbon Nanotube & Graphene Field Effect Transistors

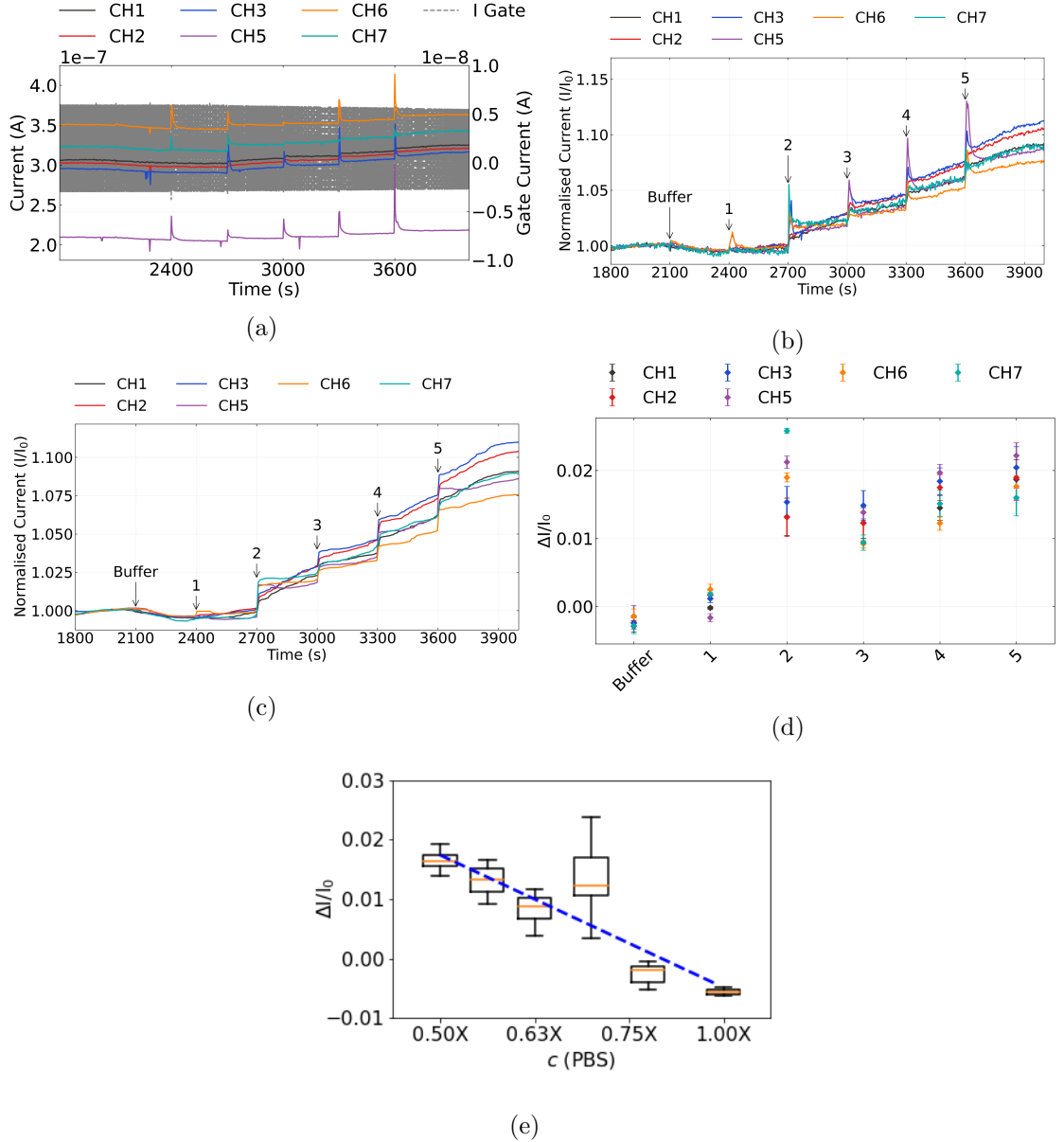


Figure 2.10.: Various visualisations of a multiplexed salt concentration sensing series taken from a single device. The source-drain voltage V_{ds} was 100 mV, and gate voltage V_g was 0 V. In (a), the raw current measurements for each channel are shown alongside gate current. The same measurements after despiking, removal of baseline drift and normalisation to initial current are shown in (b), (c) shows the data in (b) after being processed with a moving median filter, and (d) shows the signal changes in (c). The signal data in (d) is shown in box plot format in (e) alongside a fit to the median change in signal for each addition. The R squared value for the fit was 0.86.

2.4. Real-Time Salt Concentration Sensing with Phosphate Buffered Saline

drift. The mean current level just before 1800 s then becomes roughly constant. We then normalise each channel relative to their initial mean current level I_0 . We also remove artifacts resulting from PXIE-2737 module lag, single datapoints which fall well below the current level of the immediately preceding and succeeding datapoints. This ‘despike’ process uses an interquartile range filter, as discussed in Section A.4. The resulting dataset is shown in Figure 2.10b. This figure shows that the signal-to-noise ratio remains roughly similar across all channels of the device. However, the behaviour of the initial transient increase with each addition is highly variable across channels and between additions for a single channel.

As measurement of the highly variable initial transient is not useful for robust sensing purposes, we can apply a moving median filter to the dataset, discussed further in Section A.4. The filtered data is shown in Figure 2.10c. Noise and initial transients are removed completely, while the clearly defined step to a new current baseline is retained. Using the realtime data in Figure 2.10c, a plot of signal against addition can be created using the method described in Section A.4, shown in Figure 2.10d. This presentation of the data allows us to see the increase at each step relative to I_0 .

Intriguingly, even though the largest change in PBS concentration occurred at the first deionised water addition (see Table 2.7), there was very little signal change across all channels, while a relatively large change occurred at the second addition. The logarithm of final salt concentration has previously been shown to be proportional to conductance change in the linear on-regime [58]. Figure 2.10e shows the signal change presented in terms of this logarithmic relationship. We see that the median values of the first two additions do not line up well with the overall logarithmic trend. Insufficient mixing in the tightly enclosed PDMS well environment for the first few additions may be responsible for this result. Subsequent additions may improve mixing in the well, leading to the change in concentration at the surface of the channel being more representative of the overall concentration in the well.

In Figure 2.10b and Figure 2.10c, we see that the drift behaviour of individual channels begin to significantly diverge from one another from roughly the second deionised water addition onwards. This deviation from the baseline drift subtracted from the raw data occurs either because the linear fit is only a first-order approximation which weakens with time, or because the additions themselves affect the drift behaviour. Displaying the data as discrete signal changes, as in Figure 2.10d, is one way of excluding these deviations (see Section A.4). An alternative way of presenting the signal changes, by normalising relative to both I_0 and the final current reading with the formula $(I - I_0)/(I_f - I_0)$, is shown in Figure 2.11. This approach is useful for filtering out remaining unaccounted-for drift behaviour in order to compare the short-term transient responses to additions across the device channels. Furthermore, it lets us better understand how the short-term transient responses affect the longer-term step responses discussed earlier.

Figure 2.11a and Figure 2.11c show that the transient responses to DI water additions vary significantly across the surface of the device. For example, Figure 2.11c shows that in response to the second DI water addition, channel 7 gives a large initial transient

2. Characteristics of Pristine Carbon Nanotube & Graphene Field Effect Transistors

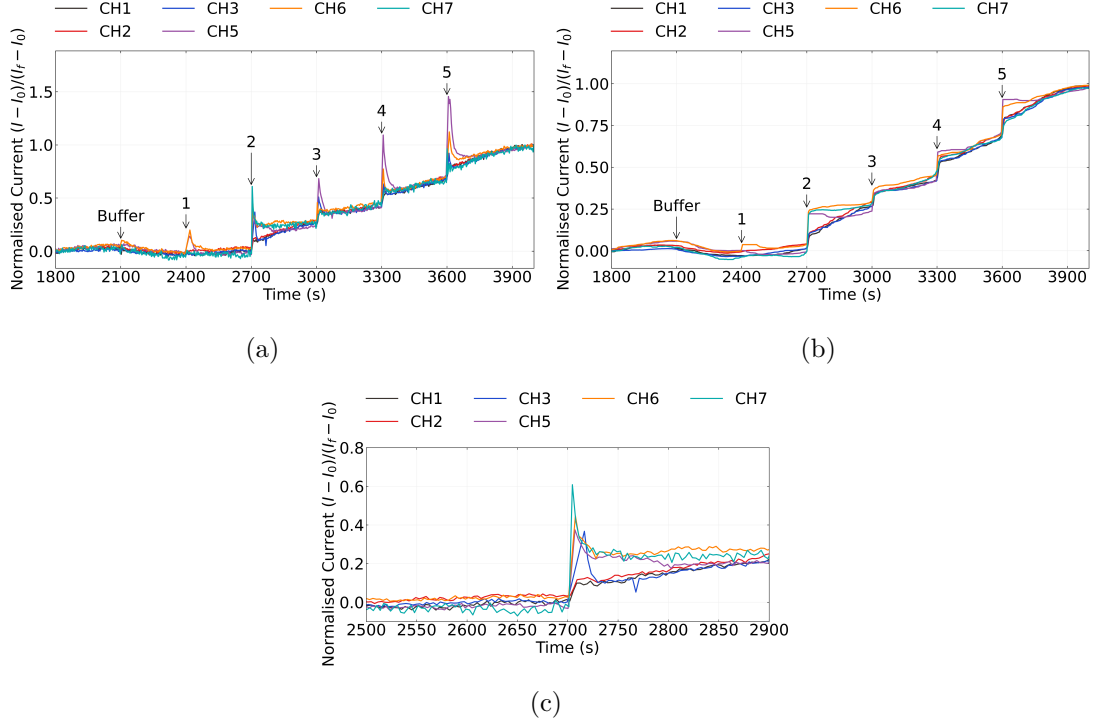


Figure 2.11.: The processed data shown in Figure 2.10b and Figure 2.10c is normalised to I_0 , but an alternative normalisation can more effectively filter out remaining drift present. This normalisation presents data relative to both I_0 and the final current reading I_f using the formula $(I - I_0)/(I_f - I_0)$. Using this normalisation, the data in Figure 2.10b and Figure 2.10c can be displayed instead as (a) and (b) respectively. (c) shows a magnified version of the step at addition 2 in (a).

2.4. Real-Time Salt Concentration Sensing with Phosphate Buffered Saline

response about twice the size of the step increase between 2600 and 2800 s. Meanwhile, channels 1 and 2 show no transient response above the step increase. Figure 2.11c indicates transient size is based on location across the device, with neighbouring channels showing the most similar behaviour. This spatially-dependent behaviour may indicate transient responses are determined by the location of the channel relative to either the location of water additions or the slightly-variable location of the liquid gate. From comparing Figure 2.11a to Figure 2.11b, we see that larger and longer-lasting transient responses are not entirely removed by the moving median filter, and so careful placement of additions is important when sensing to minimise this effect. However, even the longest-lasting transients appear to decay to zero within about 200 s, demonstrating that a 200 s spacing between additions at minimum is necessary for reliable real-time liquid-gated sensing using this setup.

Signal-to-Noise Ratio

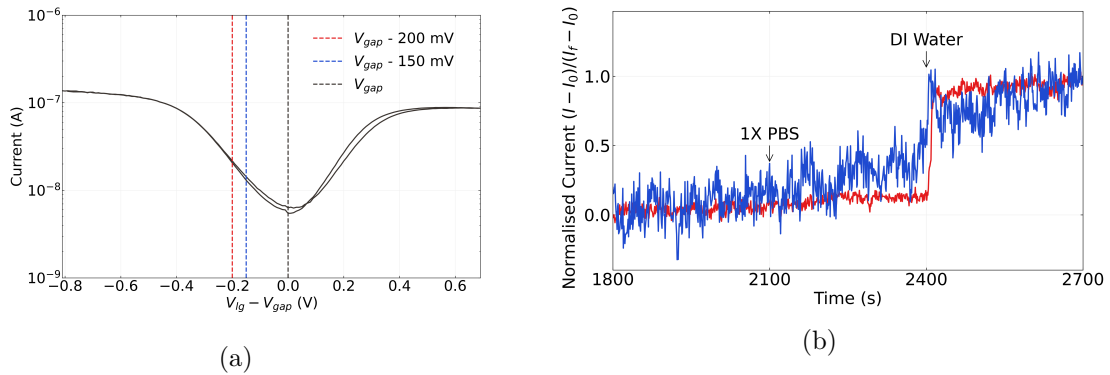


Figure 2.12.: The transfer characteristics of a single steam-deposited carbon nanotube field-effect transistor channel are shown in (a). V_{gap} is the gate voltage corresponding to the center of the transistor bandgap, found at the minimum of the characteristic curve. The signal-to-noise ratio of the channel response to a deionised water addition after a suitable control series is shown in (b). The blue current trace in (b) was performed gating the device 150 mV away from V_{gap} , while the red current was performed gating the device 200 mV away from V_{gap} .

To understand the effect of gate voltages on signal-to-noise ratio, two PBS control and salt concentration sensing series were performed with the same channel at different gate voltages. The transfer characteristics of this channel are shown in Figure 2.12a, with coloured dashed lines marking the voltages used for gating the transistor during each sensing series. Figure 2.12 shows the initial PBS and DI water additions made after 1800 s. Previous work on the signal-to-noise ratio for liquid-gated, encapsulated carbon nanotube devices suggests that gating devices close to V_{gap} should give the largest signal-to-noise ratio for salt concentration additions [40]. However, this was not what was

2. Characteristics of Pristine Carbon Nanotube & Graphene Field Effect Transistors

observed for our carbon nanotube field-effect transistor, as Figure 2.12 shows improved signal-to-noise ratio, i.e. the signal step can be more clearly distinguished, when gated at a voltage further removed from V_{gap} . This discrepancy could be a result of the use of a network of carbon nanotubes rather than a single nanotube; gating may have less of an impact on noise when a network morphology is used. Alternatively, it could be a result of a lack of mixing in our static well setup leading to inconsistent signal sizes with concentration change. Heller *et al.* used a flow cell during their signal-to-ratio work [40]. By using a flow cell with our devices we could confirm whether this is the case, and this might also help us reduce the size of unwanted transient responses resulting from drop-wise additions.

2.5. Conclusion

To ensure fabricated transistors were suitable for biosensing purposes, the morphology and electrical properties of the pristine carbon nanotube and graphene transistors were investigated.

The morphology of the carbon nanotube networks were found to have a significant impact on the electrical characteristics of the devices, which was determined through comparison of the skew-normal height profile of the carbon nanotube network and the key electrical parameters of a range of carbon nanotube devices. When networks were highly bundled ($> 90\%$), there was a large range of carbon nanotube bundle diameters present in the network. This large variation in the size of conducting pathways resulted in a wide range of on-off ratios and threshold voltages for the liquid-gated devices created using these carbon nanotube films. In contrast, devices using films fabricated with a relatively low percentage of bundling ($< 75\%$) showed highly consistent on-off ratios and threshold voltages, along with low hysteresis, due to the relatively consistent bundle diameters and high density of these networks. These low-bundling networks were found to have a mean bundle distribution height of 3.3 ± 1.0 nm. When performing multiplexed sensing, consistent channel behaviour is highly desirable since comparing sensing behaviour between channels is more straightforward.

However, atomic force microscope imaging and Raman spectroscopy also indicated that less bundled networks had the most surface contamination present. Aggregated surfactant present on the surface had a height of more than 4 nm, and introduced significant defects to the carbon nanotube network. The introduction of *p*-dopants to the carbon nanotubes by surfactant appears to have significantly increased the threshold voltage of steam-assisted surfactant-deposited network devices relative to steam-free surfactant-deposited network devices. Since the presence of surfactant could negatively impact biosensing, techniques to remove contaminants should be explored in more detail. Oxidation and thermal annealing of carbon nanotube films at high temperatures could be used to resolve this issue, and this is discussed further in ?@sec-future-work. The

2.5. Conclusion

presence of electrolyte on the surface of a backgated transistor for use in vapour sensing was also found to significantly adversely affect its electrical characteristics.

Constant voltage real-time measurements of the carbon nanotube field-effect transistor devices had a characteristic drift that could be modelled using a exponential and linear term. The linear term of baseline drift had a reasonably consistent gradient between device channels, with a mean value of -6.1 ± 1.2 , indicating that similar drift behaviour should be reproducible between devices fabricated in the same manner. The time constant of the exponential term ranged from $\tau = 330 \pm 20$ s to $\tau = 800 \pm 750$ for the device characterised. As this range of time constants falls well below the total 1800 s used for the PBS control series, we can say that the PBS control series is a suitable time length for minimising the effects of baseline drift on sensing experiments.

Salt concentration or PBS dilution sensing series indicated that the carbon nanotube transistor devices were highly sensitive to environmental changes and therefore suitable for sensing work. Successive additions of deionised water to the 1XPBS present in the well gave signal responses of up to 2.5 % above the control response. The signal response was found to be proportional to the logarithm of concentration, giving a fit to the median response sizes with an $R^2 = 0.86$. Deviations from this trend can possibly be explained by the enclosed sensing environment preventing sufficient mixing of electrolyte concentrations within the PDMS well, which could possibly be addressed by using a flow cell for sensing work. It was also seen that the signal size relative to baseline drift was highly consistent between channels. This is a promising result when it comes to ensuring consistent multiplexing, but it cannot be guaranteed that this behaviour carries over to sensing with biofunctionalised devices.

Graphene field-effect transistor devices were often found to possess a double-minima feature, which appears to be the result of a lack of doping from the metal contacts in the center of the device channels. These double Dirac points are unlikely to have an significant effect on the sensing behaviour of graphene devices. The graphene device characteristics were found to be consistent after 1 hour exposure to 1X PBS with minimal drift, with an on-off ratio of 5 and major Dirac point voltage of 0.3 V. There was some indications from the transfer characteristics that *p*-dopants were present on the graphene surface. Salt concentration sensing with graphene FETs is not shown in this thesis, but it is important to perform this experiment and use similar analysis techniques if there are any concerns about the sensitivity of a fabricated batch of graphene devices.

A. Python Code for Data Analysis

A.1. Code Repository

The code used for general analysis of field-effect transistor devices in this thesis was written with Python 3.8.8. Contributors to the code used include Erica Cassie, Erica Happe, Marissa Dierkes and Leo Browning. The code is located on GitHub and the research group OneDrive, and is available on request.

A.2. Atomic Force Microscope Histogram Analysis

The purpose of this code is to analyse atomic force microscope (AFM) images of carbon nanotube networks in .xyz format taken using an atomic force microscope and processed in Gwyddion (see Section 1.4). It was originally designed by Erica Happe in Matlab, and adapted by Marissa Dierkes and myself for use in Python. The code imports the .xyz data and sorts it into bins 0.15 nm in size for processing. To perform skew-normal distribution fits, both *scipy.optimize.curve_fit* and *scipy.stats.skewnorm* modules are used in this code.

A.3. Raman Spectroscopy Analysis

The purpose of this code is to analyse a series of Raman spectra taken at different points on a single film (see Section 1.6). Data is imported in a series of tab-delimited text files, with the low wavenumber spectrum ($100\text{ cm}^{-1} - 650\text{ cm}^{-1}$) and high wavenumber spectrum ($1300\text{ cm}^{-1} - 1650\text{ cm}^{-1}$) imported in separate datafiles for each scan location.

A.4. Field-Effect Transistor Analysis

The purpose of this code is to analyse electrical measurements taken of field-effect transistor (FET) devices. Electrical measurements were either taken from the Keysight 4156C Semiconductor Parameter Analyser, National Instruments NI-PXIe or Keysight B1500A Semiconductor Device Analyser as discussed in Section 1.7; the code is able to analyse data taken from all three measurement setups. The main Python file in the

A. Python Code for Data Analysis

code base consists of three related but independent modules: the first analyses and plots sensing data from the FET devices, the second analyses and plots transfer characteristics from channels across a device, and the third compares individual channel characteristics before and after a modification or after each of several modifications. The code base also features a separate config file and style sheet which govern the behaviour of the main code. The code base was designed collaboratively by myself and Erica Cassie over GitHub using the Sourcetree Git GUI.

The first of the three modules is for processing sensing datasets. This module imports sensing measurements in .csv format and analyses them, then outputs a plot of the raw data, alongside multiple plots which have been modified in various ways. It can also fit exponential and linear trendlines to regions of the sensing data, as well as find the signal change per analyte addition, and returns spreadsheets containing the results of these analyses. These spreadsheets include the standard deviation for all included parameters. Modified plots include normalised plots (type of normalisation can be set in config file), plots with fitted curves, plots with the linear baseline drift removed, plots of signal with analyte addition, “despiked” plots and “filtered” plots. It is possible to add annotations to any of these plots using the config file, and it is possible to produce a plot with a combination of these modifications.

The `scipy.optimize.curve_fit` module is used to fit linear and exponential curves to regions of interest of the sensing data. Initial parameters for the `scipy.optimize.curve_fit` module are chosen by approximating fitting parameters in a similar manner to the approach in Section A.2. For a linear fit $mt+b$, the parameters are simply set as $m = 1$ and $b = 0$. For an exponential fit $a \exp(-t/\tau) + c$, c is set as the final current measurement of the region of interest and a is set as the initial current measurement minus c . Then, τ is set as the time where current has dropped to $e^{-1}a + c$.

“Despiked” plots have had spurious datapoints removed through the use of an interquartile range rolling filter. The window size of the rolling filter used was 40 datapoints, and datapoints in each window with a z-score above ± 3 were removed from the plotted/processed data. “Filtered” plots had noise reduced using a moving median filter. The moving median filter is more effective at removing noise than a simple moving average, and has advantages over other filters (such as the Savitzky-Golay filter) when removing noise from data with sharp edges, as is the case for sensing data. Median filtering can also be used for baseline drift compensation, though this approach was not used in this thesis [69]. The moving median filter used had a window of 40 datapoints.

Plots of signal with analyte addition were constructed from current data after first removing baseline drift and applying a moving median filter. A simple difference calculation between the mean of the filtered current before an addition and the mean of the filtered current after the addition was performed at each addition. These differences were then normalised relative to the initial current. The signal with analyte addition give reasonably consistent results regardless of whether baseline drift was removed from the data, as shown in Figure A.1. We can therefore be confident that robust signal with analyte addition plots are robust even in the presence of significant drift.

A.4. Field-Effect Transistor Analysis

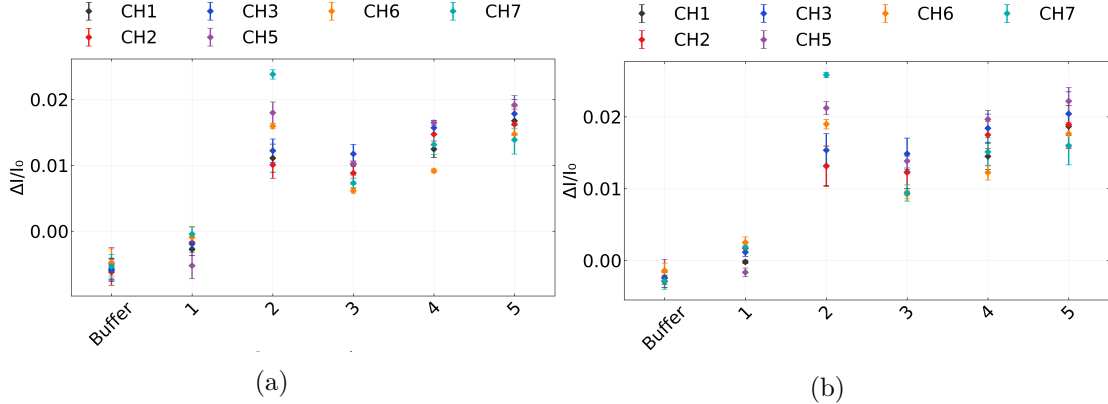


Figure A.1.: A comparison of signal with analyte addition plots taken from the same salt concentration sensing dataset (the same dataset as used in Figure 2.10). In (a), a simple difference calculation performed on filtered data was used, while in (b) the same calculation was performed on filtered data with the baseline drift removed, the method used in the body of the thesis.

The second module imports transfer measurements in .csv format and creates combined and individual plots of the eight channels on a single device. In combined plots, channels which are non-working, due to being shorted or non-conducting, are removed via setting a maximum and minimum possible on-current in the config file. Various parameters from the transfer characteristics are saved as a spreadsheet along with standard error. These parameters include on current, off current, subthreshold slope and threshold voltage for the carbon nanotube devices, and on current, off current and major Dirac point voltage for graphene devices. The device type being analysed can be set in the config file.

The third module imports several transfer measurements in .csv format and allows for comparison of the same channel before and after some modification. It also calculates the shift in either threshold voltage or major Dirac voltage of the device.

Bibliography

- [1] MicroChemicals. *Photoresists AZ and MicroChemicals TI resists*. URL: <https://www.microchemicals.com/products/photoresists.html> (visited on 2023-06-09).
- [2] Kayaku (Microchem). *SU-8 2000 Permanent Negative Epoxy Photoresist / Kayaku*. URL: <https://kayakuam.com/products/su-8-2000/> (visited on 2023-06-30).
- [3] Faris M. Albarghouthi, Nicholas X. Williams, James L. Doherty, et al. “Passivation Strategies for Enhancing Solution-Gated Carbon Nanotube Field-Effect Transistor Biosensing Performance and Stability in Ionic Solutions”. In: *ACS Applied Nano Materials* 5.10 (Oct. 2022), pp. 15865–15874. ISSN: 25740970. DOI: 10.1021/ACSANM.2C04098/SUPPL_FILE/AN2C04098_SI_001.PDF. URL: <https://doi.org/10.1021/acsanm.2c04098>.
- [4] Ziyu Chen and Jeong Bong Lee. “Biocompatibility of SU-8 and Its Biomedical Device Applications”. In: *Micromachines* 2021, Vol. 12, Page 794 12.7 (July 2021), p. 794. ISSN: 2072-666X. DOI: 10.3390/MI12070794. URL: <https://www.mdpi.com/2072-666X/12/7/794>.
- [5] Jisook Oh, Jihyun Myoung, Jin Sung Bae, et al. “Etch Behavior of ALD Al₂O₃ on HfSiO and HfSiON Stacks in Acidic and Basic Etchants”. In: *Journal of The Electrochemical Society* 158.4 (Apr. 2011), pp. D217–D222. ISSN: 0013-4651. DOI: 10.1149/1.3554729/XML. URL: <https://iopscience.iop.org/article/10.1149/1.3554729%20https://iopscience.iop.org/article/10.1149/1.3554729/meta>.
- [6] Muhammad Munem Ali, Jacob John Mitchell, Gregory Burwell, et al. “Application of Molecular Vapour Deposited Al₂O₃ for Graphene-Based Biosensor Passivation and Improvements in Graphene Device Homogeneity”. In: *Nanomaterials* 11.8 (Aug. 2021). ISSN: 20794991. DOI: 10.3390/NANO11082121. URL: [/pmc/articles/PMC8398646/](https://pmc/articles/PMC8398646/)?report=abstract%20https://www.ncbi.nlm.nih.gov/pmc/articles/PMC8398646/.
- [7] Vittorio Guarneri, Leonardo Biazi, Roberto Marchiori, et al. “Platinum metallization for MEMS application. Focus on coating adhesion for biomedical applications”. In: *Biomatter* 4.1 (Jan. 2014), e28822. ISSN: 2159-2535. DOI: 10.4161/BIOM.28822. URL: <https://pubmed.ncbi.nlm.nih.gov/24743057/>.
- [8] Thanihaichelvan Murugathas, Leo A. Browning, Marissa P. Dierkes, et al. “Data on liquid gated CNT network FETs on flexible substrates”. In: *Data in Brief* 21 (Dec. 2018), pp. 276–283. ISSN: 2352-3409. DOI: 10.1016/J.DIB.2018.09.093.

Bibliography

- [9] Thanihaichelvan Murugathas, Han Yue Zheng, Damon Colbert, et al. "Biosensing with Insect Odorant Receptor Nanodiscs and Carbon Nanotube Field-Effect Transistors". In: *ACS Applied Materials and Interfaces* 11.9 (Mar. 2019), pp. 9530–9538. ISSN: 19448252. DOI: 10.1021/ACSAMI.8B19433/ASSET/IMAGES/LARGE/AM-2018-19433U_0002.jpeg. URL: <https://pubs.acs.org/doi/full/10.1021/acsami.8b19433>.
- [10] Bajramshahe Shkodra, Mattia Petrelli, Martina Aurora Costa Angeli, et al. "Electrolyte-gated carbon nanotube field-effect transistor-based biosensors: Principles and applications". In: *Applied Physics Reviews* 8.4 (Dec. 2021), p. 41325. ISSN: 19319401. DOI: 10.1063/5.0058591 / 1076095. URL: [/aip/apr/article/8/4/041325/1076095/Electrolyte-gated-carbon-nanotube-field-effect](https://aip.org/article/8/4/041325/1076095/Electrolyte-gated-carbon-nanotube-field-effect).
- [11] Chang Young Lee, Seunghyun Balk, Jianqi Zhang, et al. "Charge transfer from metallic single-walled carbon nanotube sensor arrays". In: *Journal of Physical Chemistry B* 110.23 (June 2006), pp. 11055–11061. ISSN: 15206106. DOI: 10.1021/JP056425V / SUPPL_FILE / JP056425VSI20060322_123713.PDF. URL: <https://pubs.acs.org/doi/full/10.1021/jp056425v>.
- [12] James Kolodzey, Enam Ahmed Chowdhury, Thomas N Adam, et al. "Electrical Conduction and Dielectric Breakdown in Aluminum Oxide Insulators on Silicon". In: *IEEE TRANSACTIONS ON ELECTRON DEVICES* 47.1 (2000), p. 121.
- [13] Kenneth R. Spring and Michael W. Davidson. *Introduction to Fluorescence Microscopy / Nikon's MicroscopyU*. URL: <https://www.microscopyu.com/techniques/fluorescence/introduction-to-fluorescence-microscopy> (visited on 2023-08-18).
- [14] Rudi Rottenfusser, Erin E. Wilson, and Michael W. Davidson. *ZEISS Microscopy Online Campus / Microscopy Basics / Fluorescence Microscopy*. URL: <https://zeiss-campus.magnet.fsu.edu/articles/basics/fluorescence.html> (visited on 2023-08-18).
- [15] H. Y. Zheng and N. O.V. Plank. "Facile fabrication of carbon nanotube network thin film transistors for device platforms". In: *International Journal of Nanotechnology* 14.1-6 (2017), pp. 505–518. ISSN: 14757435. DOI: 10.1504/IJNT.2017.082473.
- [16] Thanihaichelvan Murugathas, Leo A. Browning, Marissa P. Dierkes, et al. "Metallic-semiconducting junctions create sensing hot-spots in carbon nanotube FET aptasensors near percolation". In: *Biosensors and Bioelectronics* 130 (Apr. 2019), pp. 408–413. ISSN: 0956-5663. DOI: 10.1016/J.BIOS.2018.09.021.
- [17] Hong Phan T. Nguyen, Thanihaichelvan Murugathas, and Natalie O.V. Plank. "Comparison of Duplex and Quadruplex Folding Structure Adenosine Aptamers for Carbon Nanotube Field Effect Transistor Aptasensors". In: *Nanomaterials (Basel, Switzerland)* 11.9 (Sept. 2021). ISSN: 2079-4991. DOI: 10.3390/NANO11092280. URL: <https://pubmed.ncbi.nlm.nih.gov/34578596/>.

- [18] Wim Wenseleers, Igor L. Vlasov, Etienne Goovaerts, et al. “Efficient Isolation and Solubilization of Pristine Single-Walled Nanotubes in Bile Salt Micelles”. In: *Advanced Functional Materials* 14.11 (Nov. 2004), pp. 1105–1112. ISSN: 1616-3028. DOI: 10.1002/ADFM.200400130. URL: <https://onlinelibrary.wiley.com/doi/full/10.1002/adfm.200400130%20https://onlinelibrary.wiley.com/doi/abs/10.1002/adfm.200400130%20https://onlinelibrary.wiley.com/doi/10.1002/adfm.200400130>.
- [19] Gildas Gavrel, Bruno Jousselme, Arianna Filoromo, et al. “Supramolecular Chemistry of Carbon Nanotubes”. In: (2013), pp. 95–126. DOI: 10.1007/128_2013_450.
- [20] Greg T. Hermanson. “Buckyballs, Fullerenes, and Carbon Nanotubes”. In: *Bioconjugate Techniques* (Jan. 2013), pp. 741–755. DOI: 10.1016/B978-0-12-382239-0.00016-9.
- [21] Maki Shimizu, Shunjiro Fujii, Takeshi Tanaka, et al. “Effects of surfactants on the electronic transport properties of thin-film transistors of single-wall carbon nanotubes”. In: *Journal of Physical Chemistry C* 117.22 (June 2013), pp. 11744–11749. ISSN: 19327455. DOI: 10.1021/JP3113254/SUPPL_FILE/JP3113254_SI_001.PDF. URL: <https://pubs.acs.org/doi/full/10.1021/jp3113254>.
- [22] Antonello Di Crescenzo, Valeria Ettorre, and Antonella Fontana. “Non-covalent and reversible functionalization of carbon nanotubes”. In: *Beilstein Journal of Nanotechnology* 5.1 (2014), p. 1675. ISSN: 21904286. DOI: 10.3762/BJNANO.5.178. URL: /pmc/articles/PMC4222398/%20/pmc/articles/PMC4222398/?report=abstract%20https://www.ncbi.nlm.nih.gov/pmc/articles/PMC4222398/.
- [23] Melburne C. LeMieux, Mark Roberts, Soumendra Barman, et al. “Self-sorted, aligned nanotube networks for thin-film transistors”. In: *Science* 321.5885 (July 2008), pp. 101–104. ISSN: 00368075. DOI: 10.1126/SCIENCE.1156588. URL: <https://www.science.org>.
- [24] Chang Liu and Hui Ming Cheng. “Carbon nanotubes: controlled growth and application”. In: *Materials Today* 16.1-2 (Jan. 2013), pp. 19–28. ISSN: 1369-7021. DOI: 10.1016/J.MATTOD.2013.01.019.
- [25] Dusan Vobornik, Maohui Chen, Shan Zou, et al. “Measuring the Diameter of Single-Wall Carbon Nanotubes Using AFM”. In: *Nanomaterials* 13.3 (Feb. 2023), p. 477. ISSN: 20794991. DOI: 10.3390/NANO13030477/S1. URL: <https://www.mdpi.com/2079-4991/13/3/477/htm%20https://www.mdpi.com/2079-4991/13/3/477>.
- [26] A. Azzalini and A. Capitanio. “Statistical applications of the multivariate skew normal distribution”. In: *Journal of the Royal Statistical Society Series B* 61.3 (1999), pp. 579–602. ISSN: 13697412. DOI: 10.1111/1467-9868.00194. arXiv: 0911.2093. URL: <https://ideas.repec.org/a/bla/jorssb/v61y1999i3p579-602.html>.

Bibliography

- [27] Matěj Velický, Adam J Cooper, Peter S Toth, et al. “Mechanical stability of substrate-bound graphene in contact with aqueous solutions”. In: *2D Materials* 2.2 (May 2015), p. 024011. ISSN: 2053-1583. DOI: 10.1088/2053-1583/2/2/024011. URL: <https://iopscience.iop.org/article/10.1088/2053-1583/2/2/024011%20https://iopscience.iop.org/article/10.1088/2053-1583/2/2/024011/meta>.
- [28] Erin E. Christensen, Mitesh Amin, Trevor M. Tumiel, et al. “Localized Charge on Surfactant-Wrapped Single-Walled Carbon Nanotubes”. In: *Journal of Physical Chemistry Letters* 13.46 (Nov. 2022), pp. 10705–10712. ISSN: 19487185. DOI: 10.1021/ACS.JPCLETT.2C02650. URL: <https://pubs.acs.org/doi/full/10.1021/acs.jpclett.2c02650>.
- [29] R. L. Graham, B. D. Lubachevsky, K. J. Nurmela, et al. “Dense packings of congruent circles in a circle”. In: *Discrete Mathematics* 181.1-3 (Feb. 1998), pp. 139–154. ISSN: 0012-365X. DOI: 10.1016/S0012-365X(97)00050-2.
- [30] Eckard Specht. *The best known packings of equal circles in a circle*. URL: <http://hydra.nat.uni-magdeburg.de/packing/cci/cci.html> (visited on 2023-09-11).
- [31] Robert D. Deegan, Olgica Bakajin, Todd F. Dupont, et al. “Capillary flow as the cause of ring stains from dried liquid drops”. In: *Nature* 1997 389:6653 389.6653 (1997), pp. 827–829. ISSN: 1476-4687. DOI: 10.1038/39827. URL: <https://www.nature.com/articles/39827>.
- [32] R. T. van Gaalen, C. Diddens, H. M.A. Wijshoff, et al. “Marangoni circulation in evaporating droplets in the presence of soluble surfactants”. In: *Journal of Colloid and Interface Science* 584 (Feb. 2021), pp. 622–633. ISSN: 0021-9797. DOI: 10.1016/J.JCIS.2020.10.057.
- [33] Mindy D. Bishop, Gage Hills, Tathagata Srimani, et al. “Fabrication of carbon nanotube field-effect transistors in commercial silicon manufacturing facilities”. In: *Nature Electronics* 2020 3:8 3.8 (June 2020), pp. 492–501. ISSN: 2520-1131. DOI: 10.1038/s41928-020-0419-7. URL: <https://www.nature.com/articles/s41928-020-0419-7>.
- [34] Yulia V Marchenko and Marc G Genton. “A suite of commands for fitting the skew-normal and skew-t models”. In: *The Stata Journal* 10.4 (2010), pp. 507–539.
- [35] Alexander A. Kane, Alexandra C. Ford, April Nissen, et al. “Etching of surfactant from solution-processed, type-separated carbon nanotubes and impact on device behavior”. In: *ACS Nano* 8.3 (Mar. 2014), pp. 2477–2485. ISSN: 1936086X. DOI: 10.1021/NN406065T. URL: <https://pubs.acs.org/doi/full/10.1021/nn406065t>.
- [36] Millie S. Dresselhaus, G. Dresselhaus, R. Saito, et al. “Raman spectroscopy of carbon nanotubes”. In: *Physics Reports* 409.2 (Mar. 2005), pp. 47–99. ISSN: 0370-1573. DOI: 10.1016/J.PHYSREP.2004.10.006.

- [37] Benjamin King and Balaji Panchapakesan. "Vacuum filtration based formation of liquid crystal films of semiconducting carbon nanotubes and high performance transistor devices". In: *Nanotechnology* 25.17 (Apr. 2014), p. 175201. ISSN: 0957-4484. DOI: 10.1088/0957-4484/25/17/175201. URL: <https://iopscience.iop.org/article/10.1088/0957-4484/25/17/175201%20https://iopscience.iop.org/article/10.1088/0957-4484/25/17/175201/meta>.
- [38] M. Świniarski, A. Dużyńska, A. P. Gertych, et al. "Determination of the electronic transport in type separated carbon nanotubes thin films doped with gold nanocrystals". In: *Scientific Reports* 2021 11:1 11.1 (Aug. 2021), pp. 1–7. ISSN: 2045-2322. DOI: 10.1038/s41598-021-96307-6. URL: <https://www.nature.com/articles/s41598-021-96307-6>.
- [39] Douglas R. Kauffman and Alexander Star. "Electronically monitoring biological interactions with carbon nanotube field-effect transistors". In: *Chemical Society Reviews* 37.6 (May 2008), pp. 1197–1206. ISSN: 1460-4744. DOI: 10.1039/B709567H. URL: <https://pubs.rsc.org/en/content/articlehtml/2008/cs/b709567h%20https://pubs.rsc.org/en/content/articlelanding/2008/cs/b709567h>.
- [40] Iddo Heller, Jaan Männik, Serge G. Lemay, et al. "Optimizing the signal-to-noise ratio for biosensing with carbon nanotube transistors". In: *Nano Letters* 9.1 (Jan. 2009), pp. 377–382. ISSN: 15306984. DOI: 10.1021/NL8031636/SUPPL_FILE/NL8031636_SI_001.PDF. URL: <https://pubs.acs.org/doi/full/10.1021/nl8031636>.
- [41] Woo Jong Yu, Un Jeong Kim, Bo Ram Kang, et al. "Adaptive Logic Circuits with Doping-Free Ambipolar Carbon Nanotube Transistors". In: *NANO LETTERS* 9.4 (2009), pp. 1401–1405. DOI: 10.1021/nl803066v. URL: <https://pubs.acs.org/sharingguidelines>.
- [42] Vladimir Derenskyi, Widianta Gomulya, Jorge Mario Salazar Rios, et al. "Carbon Nanotube Network Ambipolar Field-Effect Transistors with 108 On/Off Ratio". In: *Advanced Materials* 26.34 (Sept. 2014), pp. 5969–5975. ISSN: 15214095. DOI: 10.1002/ADMA.201401395.
- [43] Eric Pop, Sumit Dutta, David Estrada, et al. "Avalanche, Joule breakdown and hysteresis in carbon nanotube transistors". In: *IEEE International Reliability Physics Symposium Proceedings* (2009), pp. 405–408. ISSN: 15417026. DOI: 10.1109/IRPS.2009.5173287.
- [44] Nima Rouhi, Dheeraj Jain, Katayoun Zand, et al. "Fundamental limits on the mobility of nanotube-based semiconducting inks". In: *Advanced Materials* 23.1 (Jan. 2011), pp. 94–99. ISSN: 09359648. DOI: 10.1002/ADMA.201003281.
- [45] Jana Zaumseil. "Single-walled carbon nanotube networks for flexible and printed electronics". In: *Semiconductor Science and Technology* 30.7 (June 2015), p. 074001. ISSN: 0268-1242. DOI: 10.1088/0268-1242/30/7/074001. URL: <https://iopscience.iop.org/article/10.1088/0268-1242/30/7/074001%20https://iopscience.iop.org/article/10.1088/0268-1242/30/7/074001/meta>.

Bibliography

- [46] Xuan P A Gao, Gengfeng Zheng, and Charles M Lieber. “Subthreshold Regime has the Optimal Sensitivity for Nanowire FET Biosensors”. In: (2010). DOI: 10.1021/nl9034219. URL: <https://pubs.acs.org/sharingguidelines>.
- [47] Donghun Kang, Noejung Park, Ju Hye Ko, et al. “Oxygen-induced p-type doping of a long individual single-walled carbon nanotube”. In: *Nanotechnology* 16.8 (May 2005), p. 1048. ISSN: 0957-4484. DOI: 10.1088/0957-4484/16/8/008. URL: <https://iopscience.iop.org/article/10.1088/0957-4484/16/8/008%20https://iopscience.iop.org/article/10.1088/0957-4484/16/8/008/meta>.
- [48] Iddo Heller, Anne M. Janssens, Jaan Männik, et al. “Identifying the mechanism of biosensing with carbon nanotube transistors”. In: *Nano Letters* 8.2 (Feb. 2008), pp. 591–595. ISSN: 15306984. DOI: 10.1021/NL072996I/SUPPL_FILE/NL072996ISI20071116_124235.PDF. URL: <https://pubs.acs.org/doi/full/10.1021/nl072996i>.
- [49] Yoshiyuki Nonoguchi, Atsushi Tani, Tomoko Murayama, et al. “Surfactant-driven Amphoteric Doping of Carbon Nanotubes”. In: *Chemistry - An Asian Journal* 13.24 (Dec. 2018), pp. 3942–3946. ISSN: 1861471X. DOI: 10.1002/ASIA.201801490.
- [50] Chris J. Barnett, Cathren E. Gowenlock, Kathryn Welsby, et al. “Spatial and Contamination-Dependent Electrical Properties of Carbon Nanotubes”. In: *Nano letters* 18.2 (Feb. 2018), pp. 695–700. ISSN: 1530-6992. DOI: 10.1021 / ACS . NANOLETT.7B03390. URL: <https://pubmed.ncbi.nlm.nih.gov/29257695/>.
- [51] Joon Sung Lee, Sunmin Ryu, Kwonjae Yoo, et al. “Origin of gate hysteresis in carbon nanotube field-effect transistors”. In: *Journal of Physical Chemistry C* 111.34 (Aug. 2007), pp. 12504–12507. ISSN: 19327447. DOI: 10.1021/JP074692Q/ASSET/IMAGES/LARGE/JP074692QF00003.JPG. URL: <https://pubs.acs.org/doi/full/10.1021/jp074692q>.
- [52] Sang Won Lee, Si Young Lee, Seong Chu Lim, et al. “Positive gate bias stress instability of carbon nanotube thin film transistors”. In: *Applied Physics Letters* 101.5 (July 2012). ISSN: 00036951. DOI: 10.1063/1.4740084/111432. URL: [/aip/apl/article/101/5/053504/111432/Positive-gate-bias-stress-instability-of-carbon](https://aip.org/article/101/5/053504/111432/Positive-gate-bias-stress-instability-of-carbon).
- [53] Tae Jun Ha, Daisuke Kiriya, Kevin Chen, et al. “Highly stable hysteresis-free carbon nanotube thin-film transistors by fluorocarbon polymer encapsulation”. In: *ACS Applied Materials and Interfaces* 6.11 (June 2014), pp. 8441–8446. ISSN: 19448252. DOI: 10.1021 / AM5013326 / ASSET / IMAGES / LARGE / AM - 2014-013326_0007.JPG. URL: <https://pubs.acs.org/doi/full/10.1021/am5013326>.
- [54] Woong Kim, Ali Javey, Ophir Vermesh, et al. “Hysteresis Caused by Water Molecules in Carbon Nanotube Field-Effect Transistors”. In: *NANO LETTERS* 3.2 (2003), pp. 193–198. DOI: 10.1021/nl0259232.

- [55] Aaron D. Franklin, George S. Tulevski, Shu Jen Han, et al. "Variability in carbon nanotube transistors: Improving device-to-device consistency". In: *ACS Nano* 6.2 (Feb. 2012), pp. 1109–1115. ISSN: 19360851. DOI: 10.1021/NN203516Z/SUPPL_FILE/NN203516Z_SI_001.PDF. URL: <https://pubs.acs.org/doi/full/10.1021/nn203516z>.
- [56] Helene Conseil, Morten S. Jellesen, and Rajan Ambat. "Experimental study of water absorption of electronic components and internal local temperature and humidity into electronic enclosure". In: *Proceedings of the 16th Electronics Packaging Technology Conference, EPTC 2014* (Jan. 2014), pp. 355–359. DOI: 10.1109/EPTC.2014.7028356.
- [57] I. Heller, S. Chattoor, J. Männik, et al. "Comparing the weak and strong gate-coupling regimes for nanotube and graphene transistors". In: *physica status solidi (RRL) – Rapid Research Letters* 3.6 (Sept. 2009), pp. 190–192. ISSN: 1862-6270. DOI: 10.1002/PSSR.200903157. URL: <https://onlinelibrary.wiley.com/doi/full/10.1002/pssr.200903157%20https://onlinelibrary.wiley.com/doi/abs/10.1002/pssr.200903157%20https://onlinelibrary.wiley.com/doi/10.1002/pssr.200903157>.
- [58] Iddo Heller, Sohail Chattoor, Jaan Männik, et al. "Influence of electrolyte composition on liquid-gated carbon nanotube and graphene transistors". In: *Journal of the American Chemical Society* 132.48 (Dec. 2010), pp. 17149–17156. ISSN: 00027863. DOI: 10.1021/JA104850N/SUPPL_FILE/JA104850N_SI_001.PDF. URL: <https://pubs.acs.org/doi/full/10.1021/ja104850n>.
- [59] Fengnian Xia, Damon B. Farmer, Yu Ming Lin, et al. "Graphene field-effect transistors with high on/off current ratio and large transport band gap at room temperature". In: *Nano Letters* 10.2 (Feb. 2010), pp. 715–718. ISSN: 15306984. DOI: 10.1021/NL9039636/ASSET/IMAGES/LARGE/NL-2009-039636_0003.JPG. URL: <https://pubs.acs.org/doi/full/10.1021/nl9039636>.
- [60] Dmitry Kireev, Max Brambach, Silke Seyock, et al. "Graphene transistors for interfacing with cells: towards a deeper understanding of liquid gating and sensitivity". In: *Scientific Reports* 2017 7:1 7.1 (July 2017), pp. 1–12. ISSN: 2045-2322. DOI: 10.1038/s41598-017-06906-5. URL: <https://www.nature.com/articles/s41598-017-06906-5>.
- [61] Antonio Di Bartolomeo, Filippo Giubileo, Salvatore Santandrea, et al. "Charge transfer and partial pinning at the contacts as the origin of a double dip in the transfer characteristics of graphene-based field-effect transistors". In: *Nanotechnology* 22.27 (May 2011), p. 275702. ISSN: 0957-4484. DOI: 10.1088/0957-4484/22/27/275702. URL: <https://iopscience.iop.org/article/10.1088/0957-4484/22/27/275702%20https://iopscience.iop.org/article/10.1088/0957-4484/22/27/275702/meta>.
- [62] Zengguang Cheng, Qiaoyu Zhou, Chenxuan Wang, et al. "Toward intrinsic graphene surfaces: A systematic study on thermal annealing and wet-chemical treatment of SiO₂-supported graphene devices". In: *Nano Letters* 11.2 (Feb. 2011), pp. 767–771. ISSN: 15306984. DOI: 10.1021/NL103977D/SUPPL_FILE/

Bibliography

- NL103977D_SI_001.PDF. URL: <https://pubs.acs.org/doi/full/10.1021/nl103977d>.
- [63] Dong Wook Shin, Hyun Myoung Lee, Seong Man Yu, et al. “A facile route to recover intrinsic graphene over large scale”. In: *ACS Nano* 6.9 (Sept. 2012), pp. 7781–7788. ISSN: 19360851. DOI: 10.1021/NN3017603/SUPPL_FILE/NN3017603_SI_001.PDF. URL: <https://pubs.acs.org/doi/full/10.1021/nn3017603>.
 - [64] Tingting Feng, Dan Xie, Jianlong Xu, et al. “Back-gate graphene field-effect transistors with double conductance minima”. In: *Carbon* 79.1 (Nov. 2014), pp. 363–368. ISSN: 0008-6223. DOI: 10.1016/J.CARBON.2014.07.078.
 - [65] Song ang Peng, Zhi Jin, Dayong Zhang, et al. “How Do Contact and Channel Contribute to the Dirac Points in Graphene Field-Effect Transistors?” In: *Advanced Electronic Materials* 4.8 (Aug. 2018), p. 1800158. ISSN: 2199-160X. DOI: 10.1002/AELM.201800158. URL: <https://onlinelibrary.wiley.com/doi/full/10.1002/aelm.201800158%20https://onlinelibrary.wiley.com/doi/abs/10.1002/aelm.201800158%20https://onlinelibrary.wiley.com/doi/10.1002/aelm.201800158>.
 - [66] Y. Bargaoui, M. Troudi, P. Bondavalli, et al. “Gate bias stress effect in single-walled carbon nanotubes field-effect-transistors”. In: *Diamond and Related Materials* 84 (Apr. 2018), pp. 62–65. ISSN: 0925-9635. DOI: 10.1016/J.DIAMOND.2018.03.011.
 - [67] Steven G. Noyce, James L. Doherty, Zhihui Cheng, et al. “Electronic Stability of Carbon Nanotube Transistors under Long-Term Bias Stress”. In: *Nano Letters* 19.3 (Mar. 2019), pp. 1460–1466. ISSN: 15306992. DOI: 10.1021/ACS.NANOLETT.8B03986/ASSET/IMAGES/LARGE/NL-2018-03986G_0005.JPG. URL: <https://pubs.acs.org/doi/full/10.1021/acs.nanolett.8b03986>.
 - [68] H. Lin and S. Tiwari. “Localized charge trapping due to adsorption in nanotube field-effect transistor and its field-mediated transport”. In: *Applied Physics Letters* 89.7 (Aug. 2006), p. 73507. ISSN: 00036951. DOI: 10.1063/1.2337104/332595. URL: [/aip/apl/article/89/7/073507/332595/Localized-charge-trapping-due-to-adsorption-in](https://aip/apl/article/89/7/073507/332595/Localized-charge-trapping-due-to-adsorption-in).
 - [69] David C. Stone. “Application of median filtering to noisy data”. In: 73.10 (Oct. 2011), pp. 1573–1581. ISSN: 0008-4042. DOI: 10.1139/V95-195. URL: <https://cdnsciencepub.com/doi/10.1139/v95-195>.